On the robustness of variational multiscale error estimators for the forward propagation of uncertainty

Oriol Colomés[a], Guglielmo Scovazzi[a,*], Johann Guilleminot[a]

[a] *Department of Civil and Environmental Engineering, Duke University, Durham, North Carolina 27708, USA.*

Abstract

The numerical simulation of physical phenomena and engineering problems can be affected by numerical errors and various types of uncertainties. Characterizing the former in computational frameworks involving system parameter uncertainties becomes a key issue. In this work, we study the behavior of new variational multiscale (VMS) error estimators for the propagation of parametric uncertainties in a Convection-Diffusion-Reaction (CDR) problem. A sensitivity analysis is performed to assess the performance of the error estimator with respect to the mesh discretization and physical parameters (here, the viscosity value and advection velocity). Three different manufactured analytical solutions are considered as benchmarking tests. Next, the performance of the VMS error estimators is evaluated for the CDR problem with uncertain input parameters. For this purpose, two probabilistic models are constructed for the viscosity and advection direction, and the uncertainties are propagated using a polynomial chaos expansion approach. A convergence analysis is specifically carried out for different configurations, corresponding to regimes where the CDR operator is either smooth or non-smooth. An assessment of the proposed error estimator is finally conducted for the three tests, considering both the viscous- and convection-dominated regimes.

Keywords: Variational multiscale method; a posteriori error estimation; convection-diffusion-reaction equation; uncertainty propagation.

1. Introduction

The numerical simulation of physical phenomena has found widespread applications in the engineering sciences, and relies on approximating the state of a system with an approximate state, called numerical solution hereinafter. Let ϕ_{true} be a quantity of interest that represents a certain physical phenomena, e.g. the velocity field of a fluid. Let ϕ_{mod} be the quantity of interest given by the mathematical model that describes the physical phenomena. The numerical solution is computed on a certain mesh that discretizes a given domain with a certain characteristic size, h. We will denote as ϕ_h the numerical solution of the quantity of interest ϕ_{mod}. Following [1], we can distinguish between two types of error that are responsible of the difference between the true solution and the numerical solution (ε): the numerical error, ε_{num}, and the model error, ε_{mod}, related as

$$\varepsilon_{\text{num}} = \phi_{\text{mod}} - \phi_h, \tag{1a}$$

$$\varepsilon_{\text{mod}} = \phi_{\text{true}} - \phi_{\text{mod}}, \tag{1b}$$

$$\varepsilon = \phi_{\text{true}} - \phi_h = \varepsilon_{\text{mod}} + \varepsilon_{\text{num}}. \tag{1c}$$

*Corresponding author: Guglielmo Scovazzi. Email: guglielmo.scovazzi@duke.edu, Phone: +1 (919) 660-5075, Fax: +1 (919) 660-5219

Email addresses: oriol.colomes@duke.edu (Oriol Colomés), guglielmo.scovazzi@duke.edu (Guglielmo Scovazzi), johann.guilleminot@duke.edu (Johann Guilleminot)

The numerical error includes the discretization error (both in space and time), denoted as $\varepsilon_{\text{disc}}$, the iterative convergence error, $\varepsilon_{\text{conv}}$, and round-off error, $\varepsilon_{\text{roun}}$. In order to determine the error of the numerical approximation, each source of error should be taken into account, i.e. $\varepsilon_{\text{num}} = \varepsilon_{\text{disc}} + \varepsilon_{\text{conv}} + \varepsilon_{\text{roun}}$. In practical situations, the convergence and round-off errors are small and easy to determine, therefore, the numerical error will be dominated by the discretization error. In what follows, we will not distinguish between numerical and discretization error, assuming that $\varepsilon_{\text{num}} \approx \varepsilon_{\text{disc}}$. From (1c), we also see that the true solution is approximated by the numerical solution up to an error, $\phi_{\text{true}} = \phi_h + \varepsilon$. Since, in general, one cannot obtain an exact value of the error, the numerical solution reproduces the true solution with an associated uncertainty. The characterization of this uncertainty is crucial for decision making in many engineering problems and can be addressed using Uncertainty Quantification (UQ) techniques [2].

Different approaches can be used to characterize the numerical uncertainty on a given simulation. One of them is the use of deterministic error estimators, see e.g., [3, 4], in which an approximation of the discretization error is obtained *a posteriori*, for a given solution. Another approach was proposed in [5], where the numerical error uncertainty is defined as a nonlinear function depending on the discretization error, the error on the measurement of the input data, and the error produced by the uncertainty propagation method. In this research, we focus on the definition of a family of deterministic error estimators to characterize the discretization error. Two different groups of discretization error estimators are usually distinguished in the literature, see [6]. A first group based on the use of more accurate solutions, e.g., Richardson extrapolation, see for instance [7] and references therein. The second group of numerical error estimators are based on the residual of the partial differential equation (PDE) that models the problem, e.g., adjoint methods. The error estimators described in this paper can be included into the second group. Since the first developments on the definition of *a posteriori* error estimators done by Babuska and Rheinboldt in [8], many works have been published during the last few decades. In [9] a wide overview of *a posteriori* error estimator for FE is given. Other reviews on *a posteriori* error estimators can be found, for instance, in [6, 10]. In [11] Hauke and coworkers introduced the variational multiscale (VMS) method [12] for the *a posteriori* error estimation of numerical simulations. This approach was then extended to multi-dimensional transport problems [13], and to the Euler and Navier-Stokes equations [14]. Recently, a point-wise error estimator based on VMS error estimators has also been proposed [15], and its extension to a FV framework has been proposed in [16].

The aim of this paper is twofold. First, we propose to define a new variation of the VMS error estimators based on orthogonal subscales, a concept introduced by Codina in [17], for the convection-diffusion-reaction (CDR) problem. In a recent work, Baiges *et al.* [18] developed similar error estimators based on the energy norm for the solid mechanics problem. Note that error estimators based on L^r-norms will be considered hereinafter, in contrast with the derivations in [18]. Next, we investigate the behavior of the proposed error estimators when the coefficients in the CDR problem are made random. It should be noticed that since this work is not concerned with mesh adaptivity, results will be presented on the values of the global error estimator (rather than on the distribution of the numerical error over the physical domain).

The document is organized as follows. After the introduction, the preliminary definitions are given in Section 2, with the boundary value problem definition and the description of the VMS method. In Section 3 we describe the new error estimators based on orthogonal subscales. Some numerical results in a deterministic setting are given in Section 4 for three different tests. In Section 5 the effect of uncertain input parameters over the defined error estimators is assessed. Finally, some conclusions are pointed out in Section 6.

2. Preliminaries

2.1. The boundary value problem

Let us consider the spatial domain Ω with boundaries $\Gamma_D \cup \Gamma_N = \Gamma$, being Γ_D the Dirichlet (essential) boundary and Γ_N the Neumann (natural) boundary, and $\Gamma_D \cap \Gamma_N = \emptyset$. The strong form of the steady convection-diffusion-reaction (CDR) problem reads:

Find u such that

$$\begin{aligned} -\nu\Delta u + \mathbf{a}\cdot\nabla u + su &= f \qquad \text{in } \Omega, \\ u &= g \qquad \text{on } \Gamma_D, \\ \mathcal{B}u &= h \qquad \text{on } \Gamma_N, \end{aligned} \tag{2}$$

where ν is the viscosity, $\mathbf{a}$ the advection velocity, s the reaction, g a given function defined on the Dirichlet boundary Γ_D, h a given function defined on the boundary Γ_N and f the external source term defined in Ω. Furthermore, $\mathcal{B}u$ is the Neumann boundary operator acting over u, defined as $\mathcal{B}u := \nu\nabla u\cdot\mathbf{n}$. Let us define the CDR operator as

$$\mathcal{L}u := -\nu\Delta u + \mathbf{a}\cdot\nabla u + su. \tag{3}$$

Some notation has to be defined before we proceed with the derivation of the weak problem. We denote by $L^p(\Omega)$, $1 \le p < \infty$, the spaces of functions such that their p-th power is absolutely integrable in Ω. For the case in which $p = 2$, we have a Hilbert space with scalar product

$$(u, v)_\Omega \equiv (u, v) := \int_\Omega u(\mathbf{x})\, v(\mathbf{x})\, d\Omega \tag{4}$$

and induced norm $\|u\|_{L^2(\Omega)} \equiv \|u\| = (u, u)^{1/2}$. The space of functions whose distributional derivatives up to order m are in $L^2(\Omega)$ are denoted by $H^m(\Omega)$. We will focus on the case of $m = 1$, which is also a Hilbert space. $H^1_0(\Omega)$ is the set of functions in $H^1(\Omega)$ that have zero trace on Γ_D, and $H^1_g(\Omega)$ the set of functions $u \in H^1(\Omega)$ such that $u = g$ on Γ_D. The weak form of the problem (2) can be stated as:

Find $u \in \mathcal{V}_g$ such that

$$a(v, u) = (v, f) + (v, h)_{\Gamma_N} \qquad \forall v \in \mathcal{V}_0, \tag{5}$$

where $a(\cdot,\cdot)$ is the bilinear form defined as

$$a(v, u) := (v, \mathcal{L}u) + (v, \mathcal{B}u)_{\Gamma_N}, \tag{6}$$

and the variational spaces $\mathcal{V}_g$ and $\mathcal{V}_0$ are defined as

$$\mathcal{V}_g := \{v \in H^1(\Omega) : v|_{\Gamma_D} = g\} \equiv H^1_g(\Omega), \tag{7}$$

$$\mathcal{V}_0 := \{v \in H^1(\Omega) : v|_{\Gamma_D} = 0\} \equiv H^1_0(\Omega). \tag{8}$$

Let us consider a finite element partition $\mathcal{T}_h$ of the domain Ω from which we can construct a conforming Finite Element (FE) space $\mathcal{V}_h \subset \mathcal{V}$. Let $\mathcal{E}_h = \cup_{K\in\mathcal{T}_h}\partial K$ be the set of the faces (or edges in 2D) of the mesh and $\mathcal{E}^0_h = \mathcal{E}_h\backslash\Gamma$. The FE spaces equivalent to (7)-(8) can be defined as

$$\mathcal{V}_{g,h} := \{v_h \in \mathcal{V}_h : v_h|_{K\cap\Gamma_D} = g\}, \tag{9}$$

$$\mathcal{V}_{0,h} := \{v_h \in \mathcal{V}_h : v_h|_{K\cap\Gamma_D} = 0\}. \tag{10}$$

The Galerkin FE approximation of (5) consists in finding $u_h \in \mathcal{V}_{g,h}$ such that

$$a(v_h, u_h) = (v_h, f) + (v_h, h)_{\Gamma_N} \qquad \forall v_h \in \mathcal{V}_{0,h}. \tag{11}$$

2.2. The variational multiscale method

It is well known that the Galerkin approximation obtained solving (11) suffers from numerical instabilities in the convection-dominated regime. In order to overcome this issue, the variational multiscale stabilization can be adopted (see Hughes [12]), as outlined in what follows.

Let us consider a decomposition of the variational space $\mathcal{V} = \mathcal{V}_h \oplus \mathcal{V}'$ into the space of resolved scales $\mathcal{V}_h$ (associated with the FE solution) and the space of unresolved scales $\mathcal{V}'$ (associated with the

error). Applying this decomposition to the solution $u = u_h + u'$ and the test function $v = v_h + v'$, and introducing the result into (5) we obtain the following weak problems.

$$a(v_h, u_h) = -a(v_h, u') + (v_h, f) + (v_h, h)_{\Gamma_N} \qquad \forall v_h \in \mathcal{V}_{0,h}, \tag{12}$$

$$a(v', u') = -a(v', u_h) + (v', f) + (v', h)_{\Gamma_N} \qquad \forall v' \in \mathcal{V}'_0. \tag{13}$$

Problem (12) can be solved since $\mathcal{V}_h$ is a finite-dimensional space, but problem (13) is defined in an infinite-dimensional space, and for this reason is in general not computable.

Equation (13) can be used to approximate u' in terms of the residual of the CDR operator acting on the finite element component u_h [12]:

$$u' \approx \tau \mathcal{P}(f - \mathcal{L}u_h), \tag{14}$$

where $\mathcal{P}$ is a certain projection into the space of the subscales and τ an intrinsic time-scale (which has the meaning of an approximation to the fine-scale Green's function). In this work, we will consider the definition of the stabilization parameter given by [19]:

$$\tau = \left(\frac{c_1 \nu}{h^2} + \frac{c_2 |\mathbf{a}|}{h} + |s| \right)^{-1}, \tag{15}$$

with c_1 and c_2 two algorithmic constants, usually taken as $c_1 = 4$ and $c_2 = 2$. Alternative definitions can be found in [20, 21, 13].

Remark. Different choices of the elemental characteristic length h can be made. For instance, we will consider the volumetric element length, $h_{vol} := (meas(K)^{1/d})$, for the viscous effects, i.e. $h = h_{vol}$ in the terms in which there appear the viscosity, ν, in equation (15). We will instead consider the elemental length along the flow direction for the advective terms, i.e. $h = h_{\mathbf{a}}$ in the term $c_2|\mathbf{a}|/h$ in (15).

Integrating by parts the term $a(v_h, u')$ on (12), we obtain

$$a(u_h, v_h) + \sum_{K \in \mathcal{T}_h} (u', \mathcal{L}^* v_h)_K = (f, v_h) + (v_h, h)_{\Gamma_N} \quad \forall v_h \in \mathcal{V}_{0,h}, \tag{16}$$

where $\mathcal{L}^* w := -\nu \Delta w - \mathbf{a} \cdot \nabla w + sw$ is the adjoin operator of the CDR problem. Now, equation (16) can be solved making use of the approximation (14).

The choice of the subscales subspace $\mathcal{V}'$ has not been discussed yet. The *standard VMS* method (often also denoted by algebraic subgrid scales (ASGS) method, [17, 22]) assumes that the projection is the identity operator, $\mathcal{P} \equiv \mathcal{I}$, making the subscales dependent on the full residual. In this work we will also consider the case in which the subscales space is defined to be orthogonal to the FE space, i.e. $\mathcal{V}' = \mathcal{V}_h^{\perp}$. This concept was introduced by Codina in [17] and in that case, the projection appearing in (14) would be defined as $\mathcal{P} := \Pi_h^{\perp} = (\mathcal{I} - \Pi_h)$. Where $\mathcal{I}$ is the identity and Π_h is the projection into the FE space. In what follows, we will denote the orthogonal subscales method as *OSS*, for which (14) is replaced by

$$u' \approx \tau \Pi_h^{\perp}(f - \mathcal{L}u_h). \tag{17}$$

The definition of the projection operator, $\Pi_h^{\perp}$, is discussed in Appendix A.

3. Variational multiscale error estimator based on orthogonal subscales

The small scale component u' of the solution introduced in the VMS method can be understood as the numerical error of our problem, that is, $\varepsilon_{\text{num}} = u - u_h = u'$. Then, an estimate for u' is nothing else than an error estimate of the numerical solution.

As mentioned on the introduction, the definition of error estimators based on the VMS approach was first introduced by Hauke in [11], and extended to various applications in [13, 14, 23]. A definition

of an error estimator using the OSS approach has been recently proposed in [18], based on the energy norm, for solid mechanics.

In this work, we propose an error estimator definition based on L^r-norms using the OSS formulation for the CDR problem, equivalent to the definition proposed in [13], derived next. The following assumptions, typically used in the literature [12, 17], will be used in the definition of the error estimators:

***Assumption* 1.** In a given element $K \in \mathcal{T}_h$ with boundary ∂K, the subscales are local and can be expressed as bubble functions, that is, they vanish on the element boundary

$$v'(\mathbf{x}) = 0 \quad \forall \mathbf{x} \in \partial K, \forall v' \in \mathcal{V}'. \tag{18}$$

***Assumption* 2.** The subscales fluxes are continuous in the inter-element boundaries, that is,

$$[\![\mathcal{B}v']\!] = 0 \quad \forall v' \in \mathcal{V}'. \tag{19}$$

Let us start from the subscale weak problem (13). Introducing the bilinear form definition (5) into the RHS term of equation (13), integrating element by element and integrating by parts the viscous term, we have that

$$a(v', u') = (v', f - \mathcal{L}u_h)_{\widetilde{\Omega}} - (v', [\![\mathcal{B}u_h]\!])_{\widetilde{\Gamma}} - (v', \mathcal{B}u_h - h)_{\Gamma_h} \quad \forall v' \in \mathcal{V}'_0. \tag{20}$$

Now, if we define the subscales space to be orthogonal to the FE space (see Appendix A), any function belonging to the FE space, $\xi_h \in \mathcal{V}_h$, satisfies

$$(v', \xi_h)_{\widetilde{\Omega}} = 0 \quad \forall v' \in \mathcal{V}'. \tag{21}$$

In particular, making use of (21), the orthogonal projection of the residual can be subtracted to (20) and the following equation still holds

$$a(v', u') = (v', f - \mathcal{L}u_h - \Pi_h(f - \mathcal{L}u_h))_{\widetilde{\Omega}} - (v', [\![\mathcal{B}u_h]\!])_{\widetilde{\Gamma}} - (v', \mathcal{B}u_h - h)_{\Gamma_h} \quad \forall v' \in \mathcal{V}'_0. \tag{22}$$

Using Assumptions 1 and 2, and introducing the Green's function, g', for the dual problem, see [12, 24], we obtain an analytical expression for the subscales

$$u'(\mathbf{x}) = \int_{\widetilde{\Omega}} g'(\mathbf{x}, \mathbf{y})(f - \mathcal{L}u_h - \Pi_h(f - \mathcal{L}u_h))(\mathbf{y}) d\Omega - \int_{\widetilde{\Gamma}} g'(\mathbf{x}, \mathbf{y})([\![\mathcal{B}u_h]\!])(\mathbf{y}) d\Gamma - \int_{\Gamma} g'(\mathbf{x}, \mathbf{y})(\mathcal{B}u_h - h)(\mathbf{y}) d\Gamma. \tag{23}$$

Then, the small scales can be split into the element interior contributions (denoted as u'_K) and the inter-element boundary contribution (denoted as $u'_{\partial K}$), leading to

$$u'(\mathbf{x}) = u'_K(\mathbf{x}) + u'_{\partial K}(\mathbf{x}), \tag{24}$$

with

$$u'_K(\mathbf{x}) = \int_{\widetilde{\Omega}} g'(\mathbf{x}, \mathbf{y})(f - \mathcal{L}u_h - \Pi_h(f - \mathcal{L}u_h))(\mathbf{y}) d\Omega, \tag{25}$$

$$u'_{\partial K}(\mathbf{x}) = -\int_{\widetilde{\Gamma}} g'(\mathbf{x}, \mathbf{y})([\![\mathcal{B}u_h]\!])(\mathbf{y}) d\Gamma - \int_{\Gamma} g'(\mathbf{x}, \mathbf{y})(\mathcal{B}u_h - h)(\mathbf{y}) d\Gamma. \tag{26}$$

Following the procedures described in [13], for a given L^r-norm, $\|\cdot\|_{L^r(\Omega)}$, with $r \in \mathbb{N}$, we can obtain an upper bound for the subscales in terms of the interior and inter-element norms. This is achieved making use of the triangle inequality for equation (24) leading to

$$\|u'(\mathbf{x})\|_{L^r(\Omega)} \leq \|u'_K(\mathbf{x})\|_{L^r(\Omega)} + \|u'_{\partial K}(\mathbf{x})\|_{L^r(\Omega)}. \tag{27}$$

Hence, in order to have an upper bound for the error u', it is sufficient to find an upper bound for u'_K and $u'_{\partial K}$.

Remark. Other norms can be considered to construct an error estimator using the VMS approach, as it has been shown in [25], but there it is argued that, for fluid dynamics and convection-diffusion problems, L^r-norms are more suitable to construct *a posteriori* error estimators. In particular, the construction of robust *a posteriori* error estimators based on upper bounds of the elemental energy norm result in a dependency on the Péclet number in the definition of the error estimator, see [26].

To simplify the problem, we will only consider the case in which the whole domain boundary is of Dirichlet type, that is, $\Gamma \equiv \Gamma_D$. In this case, the boundary contribution will be only defined by the inter-element jumps, namely: $u'_{\partial K}(\mathbf{x}) = -\int_{\widetilde{\Gamma}} g'(\mathbf{x},\mathbf{y})([\![\mathcal{B}u_h]\!])(\mathbf{y})d\Gamma$.

3.1. Element interior bound

We can obtain a local estimate for the interior contributions by taking the L^r-norm of the subscale approximation given in equation (17). Then, at a given element $K \in \mathcal{T}_h$, we have

$$\|u'_K\|_{L^r(K)} \approx \|\tau(f - \mathcal{L}u_h - \Pi_h(f - \mathcal{L}u_h))\|_{L^r(K)}, \tag{28}$$

This approach was initially proposed in [11] and also used in [14], under the name of the *standard estimate*. Since it is an approximation, this version cannot provide an upper bound for the error.

Alternatively, as shown in [13], an upper bound for the element interior can be derived. Starting from the exact definition in (25), we approximate the global Green's function $g'(\mathbf{x},\mathbf{y})$ by an elemental Green's function $g_K(\mathbf{x},\mathbf{y})$ defined on a given element K. This approximation is justified when using the VMS approach to solve the problem, since the error distribution is local [27]. Now, taking the absolute value of (25) and applying the Hölder's inequality, we can obtain an upper bound for the interior error with the following expression

$$\|u'_K\|_{L^r(K)} \leq \left\| \|g_K(\mathbf{x},\mathbf{y})\|_{L^p(K_\mathbf{y})} \right\|_{L^r(K_\mathbf{x})} \|f - \mathcal{L}u_h - \Pi_h(f - \mathcal{L}u_h)\|_{L^q(K)}\,, \tag{29}$$

with $1 \leq p, q \leq \infty$ and $\frac{1}{p} + \frac{1}{q} = 1$. In this work we will focus on the case $p = 1$, $q = \infty$, which leads to an expression that depends on the L^∞-norm of the residual, and in particular, we will only consider the $r = 2$ case (L^2-norm of the error). According to [13], the first term on the RHS of (29) can be defined as

$$\left\| \|g_K(\mathbf{x},\mathbf{y})\|_{L^1(K_\mathbf{y})} \right\|_{L^2(K_\mathbf{x})} = \tau^K_{L^2} meas(K)^{1/2},$$

with $\tau^K_{L^2} := \min\left(\frac{h_{flow}}{\sqrt{3}|\mathbf{a}|}, \frac{h^2}{24.24\nu}, \frac{1}{|s|}\right)$. Therefore, we have an upper bound for the element interior that can be expressed as

$$\|u'_K\|_{L^2(K)} \leq \tau^K_{L^2} meas(K)^{1/2} \|f - \mathcal{L}u_h - \Pi_h(f - \mathcal{L}u_h)\|_{L^\infty(K)}\,. \tag{30}$$

Remark. In this work we use the weighted projection of the residual defined in the Appendix A, obtained through an L^2-projection onto the FE space $\mathcal{V}_h$ weighted with the stabilization parameter τ. In this case, improved results have been observed when the projection used to compute the error estimator is weighted with the parameter $\tau^K_{L^2}$. In order to reduce computational costs, the projection used to obtain the numerical solution is stored and then multiplied by a factor $\gamma := \frac{\tau^K_{L^r}}{\tau}$ to obtain the *a posteriori* error estimator.

3.2. Element boundary bound

The same procedure can be applied to obtain a bound for the contribution from the inter-element boundaries. Applying Hölder's inequality to (26) and the elemental Green's function bound described in [13], we arrive to the following expression

$$\|u'_{\partial K}\|_{L^2(K)} \leq \tau^K_{L^2} meas(K)^{1/2} \frac{1}{2} \frac{\text{meas}(\partial K)}{\text{meas}(K)} \|[\![\mathcal{B}u_h]\!]\|_{L^\infty(K)}\,. \tag{31}$$

Note that the orthogonality of the subscales is not invoked for this term, so the error estimator expression for the inter-element boundary contributions is the same as the one defined in [13].

3.3. A posteriori elemental error estimator

Introducing the element interior and the inter-element boundary bounds given in (30) and (31), respectively, into (27) we obtain a local *a posteriori* error estimator based on the OSS formulation. For a given element $K \in \mathcal{T}_h$ the proposed error estimator reads

$$\eta_K^{\text{OSS}} := \tau_{L^2}^K meas(K)^{1/2} \left(\|f - \mathcal{L}u_h - \Pi_h(f - \mathcal{L}u_h)\|_{L^\infty(K)} + \frac{1}{2} \frac{\text{meas}(\partial K)}{\text{meas}(K)} \|[\![\mathcal{B}u_h]\!]\|_{L^\infty(K)} \right). \tag{32}$$

In this work, we will compare the performance of the error estimator η_K^{OSS} with the error estimator based on the standard VMS method, defined in [13] and denoted as η_K^{VMS} hereinafter, which takes the following expression

$$\eta_K^{\text{VMS}} := \tau_{L^2}^K meas(K)^{1/2} \left(\|f - \mathcal{L}u_h\|_{L^\infty(K)} + \frac{1}{2} \frac{\text{meas}(\partial K)}{\text{meas}(K)} \|[\![\mathcal{B}u_h]\!]\|_{L^\infty(K)} \right). \tag{33}$$

Some considerations can be pointed out from the error estimator definitions (32) and (33).

Remark. On the hyperbolic limit, i.e. $\mathcal{L}u := \mathbf{a} \cdot \nabla u$, the contribution of the element interior error $\|u'_K\|_{L_r(\Omega^e)}$ is crucial. Whereas, on the elliptic limit, i.e. $\mathcal{L}u := -\nu\Delta u$, the contribution of the element boundary error $\|u'_{\partial K}\|_{L_r(\Omega^e)}$ is important.

Remark. Some comments are in order on the choice of the norms appearing in (29). As noted in [13], the choice $q = 1$ and $p = \infty$ would lead to a Green's function norm that is not bounded in the convective limit when $r = 1$. Moreover, the case $p = q = 2$ is also unbounded when $r = 2$, for convection and diffusion dominated flows. The selected choice, $p = 1$ and $q = \infty$, leads to a bounded Green's function norm and it is well suited given that the Green's function may not be smooth in a multidimensional problem.

Remark. The error estimators η_K^{OSS} and η_K^{VMS} are very similar, differing in the definition of the residual in the element interiors. Mainly, the OSS version (32) only takes into account the complement of the L^2-projection of the residual onto the FE space. This is a less conservative approach, and lower values of the error are expected with respect to η_K^{VMS}, especially when the problem has a smooth solution.

Remark. The error estimator definitions given in (32) and (33) provide an upper bound of an estimated error, not an upper bound of the exact error. Hence, there still exist the possibility of underestimating the exact error.

It is important to highlight that η_K^{OSS} and η_K^{VMS} are explicit *a posteriori* error estimators. This means that given a solution u_h, the value of the error estimator can be easily evaluated without having to solve any additional system. The algorithm used to compute these error estimators is given in Appendix B.

4. Numerical results

In this section we will assess the behavior of the proposed error estimators in a deterministic setting. In order to evaluate the performance of an error estimator, we look at the efficiency index of the global error estimation. We define the global error estimator based on the L^2-norm as

$$\eta = \left(\sum_{K \in \mathcal{T}_h} \eta_K^2 \right)^{1/2}. \tag{34}$$

The efficiency index of *a posteriori* error estimate is the ratio between the estimated error and the exact error

$$I_{\text{eff}} := \frac{\eta}{\|u - u_h\|_{L^2}}. \tag{35}$$

We say that an error estimator is efficient if I_{eff} and I_{eff}^{-1} are bounded for all triangulations, $\mathcal{T}_h$. Moreover, an efficient error estimator is called robust for all kind of problems when I_{eff} and I_{eff}^{-1} are

bounded, regardless of the problem type (e.g., boundary conditions) and problem parameters. In what follows, we want to assess the efficiency and robustness of the proposed error estimator, η^{OSS}, compared against the standard VMS error estimator, η^{VMS}.

The following tests are solved using the formulation defined in equation (16), with the subscales defined as in the standard VMS method (equation (14) with $\mathcal{P} \equiv \mathcal{I}$) or as in the OSS method (equation (17)). We will favor the use of the VMS error estimator for the solutions computed with VMS formulation and the OSS error estimator for the solutions computed with the OSS method. However, an analysis on the effect of the different residual projections to the *a posteriori* error estimator will be done, looking how the efficiency of the error estimator is modified when the different formulations are used to solve the problem. Note that the OSS error estimators based on the L^r-norm have not been studied before and part of the novelty of this work relies on the assessment of *a posteriori* error estimators suited for such method. Nevertheless, a convergence test will be performed to confirm that the other VMS methods give similar results.

All the following tests have been computed using FEMPAR [28], an open source object oriented Fortran200X scientific software library. Note that the tests shown in this section are not computationally intensive and can be solved using a serial environment. However, since the error estimators are local, they can be directly used in a parallel setting.

4.1. Definition of the tests

In what follows, three different manufactured analytic solutions are tested, all of them defined in [29]. Knowing the exact solution, we can compute the exact error of the simulation, and then, the efficiency of the error estimators can be assessed.

4.1.1. Polynomial solution (problem A)

The first test that we analyse consists on a manufactured polynomial solution. We impose a forcing term such that the solution satisfies the following expression

$$u(x, y) = 100(1 - x)^2 x^2 y(1 - 2y)(1 - y). \tag{36}$$

Different viscosity values, ν, will be used with an advection velocity $\mathbf{a} = (3, 2)^T$ and a reaction term $s = 1.0$. We solve the problem on a unit square domain, $\Omega = [0, 1] \times [0, 1]$ with Dirichlet boundary conditions imposed along all the boundaries, $\Gamma_D = \partial\Omega$. In Figure 1(a) we show the solution of the problem obtained with a 128^2 linear quadrilateral elements mesh using the OSS method. Note that the analytical solution to this problem does not depend on the physical parameters, i.e. viscosity, advection velocity and reaction.

4.1.2. Boundary layer solution (problem B)

In this test we impose a manufactured analytical solution with a boundary layer. The solution is also defined in a unit square domain, $\Omega = [0, 1] \times [0, 1]$ with Dirichlet boundary conditions imposed along all the boundaries, $\Gamma_D = \partial\Omega$. Here we impose a source term such that the solution of the equation satisfies

$$u(x, y) = xy^2 - y^2 \exp\left(\frac{2(x - 1)}{\nu}\right) - x \exp\left(\frac{3(y - 1)}{\nu}\right) + \exp\left(\frac{2(x - 1) + 3(y - 1)}{\nu}\right). \tag{37}$$

As in the previous test, we consider different choices of viscosity, with an advection velocity $\mathbf{a} = (2, 3)^T$ and a reaction $s = 1.0$. Unlike the polynomial solution presented in the previous test case, here the analytical solution depends on the viscosity value, ν. The computed solution for this problem with $\nu = 1.0e - 4$ is shown in Figure 1(b).

4.1.3. Sharp inner layer solution (problem C)

Finally, the third test considered in this work consists also in a manufactured solution, representing a circular inner boundary layer. We solve the problem in a squared domain of size $\Omega = (0,1)^2$ with homogeneous boundary conditions in the whole boundary. We prescribe an analytic force term such that

$$u(x,y) = 16x(1-x)y(1-y)\left(\frac{1}{2} + \frac{\arctan\left(\frac{2}{\sqrt{\nu}}\left(0.25^2 - (x-0.5)^2 - (y-0.5)^2\right)\right)}{\pi}\right). \tag{38}$$

In that case we also consider different choices of viscosity, with an advection velocity $\mathbf{a} = (2,3)^T$ and a reaction $s = 2.0$. The analytical solution depends on the viscosity value also for this test case, and is shown in Figure 1(c) for $\nu = 1.0e-4$.

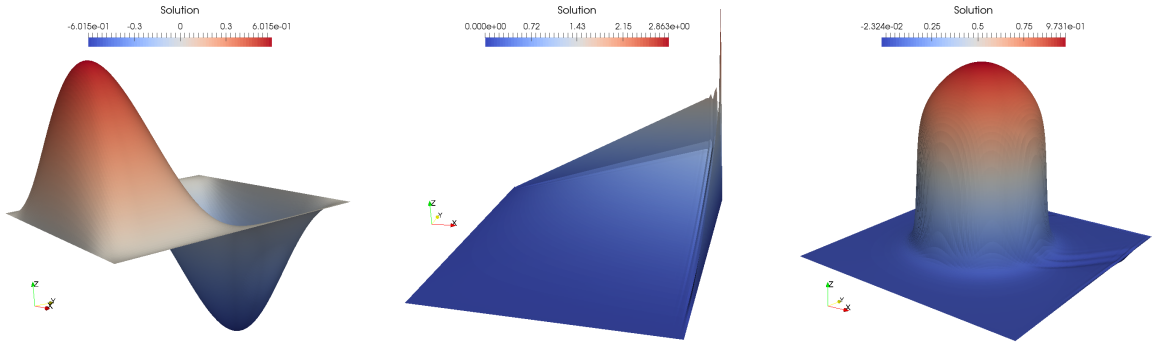

(a) *Problem A* (b) *Problem B* ($\nu = 1.0e-4$) (c) *Problem C* ($\nu = 1.0e-4$)

Figure 1: Manufactured analytical solutions used in the tests.

4.2. Mesh refinement analysis

In this section we assess the behavior of the error estimators when the mesh is refined. A first condition that an accurate error estimator has to satisfy is to match the convergence rate of the true error as the mesh size is refined. It is well known that the rate of convergence of a numerical approximation obtained using linear quadrilateral FE is $\sim h^2$. In Figure 2 we show the convergence rates for two different values of viscosity, $\nu = \{1.0, 1.0e-6\}$, with the solution computed using the OSS method defined through the subscales equation (17). The convergence rate of the error estimators matches the convergence rate of the true error, independently of the viscosity value.

As stated above, in this work we will favor the VMS error estimator, η^{VMS}, to estimate the error when the solution is computed using the standard VMS stabilization method, and the OSS error estimator, η^{OSS}, when the solution is computed using orthogonal subscales. However, in order to bring some insight on the influence of the stabilization method, we look at the efficiency index of the two error estimators evaluated from the numerical solution computed with both the VMS and OSS methods (i.e., we consider all combinations of error estimator and stabilization method). In particular, for the manufactured *polynomial solution* (probelm A), we evaluate the changes in the global efficiency of the error for different grid sizes and values of viscosity, $\nu = \{1.0, 1.0e-2, 1.0e-4, 1.0e-6\}$, see Figure 3. We recall that an efficiency index equal to one means that the estimated and true global errors match (although locally these errors may be different).

We can observe that for high viscosity values, Figure 3(a) and Figure 3(b), the proposed OSS error estimator give lower efficiencies than the standard VMS method. When the problem becomes advection-dominated, Figure 3(c) and Figure 3(d), both methods give approximately the same results.

We can also see that for viscous dominated flows ($\nu = 1.0$), the solution computed with the OSS method gives higher efficiency values, while the standard VMS stays close to 1.0. However, when the

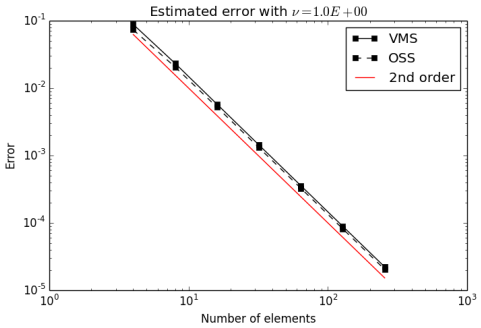

(a) $\nu = 1.0e-0$

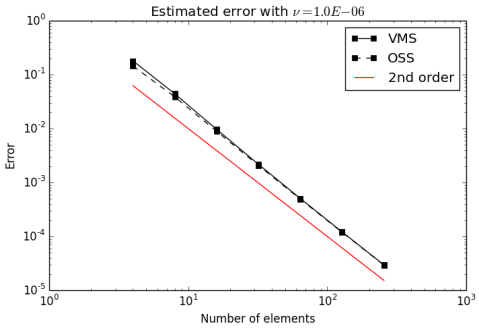

(b) $\nu = 1.0e-6$

Figure 2: *Problem A*. error estimators convergence rate for different viscosity values.

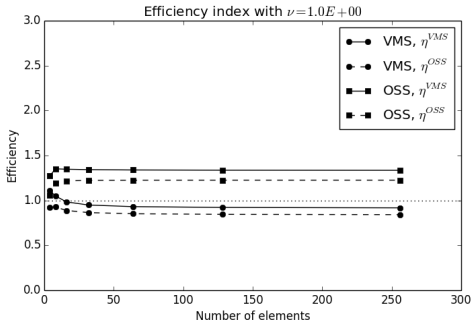

(a) $\nu = 1.0e-0$

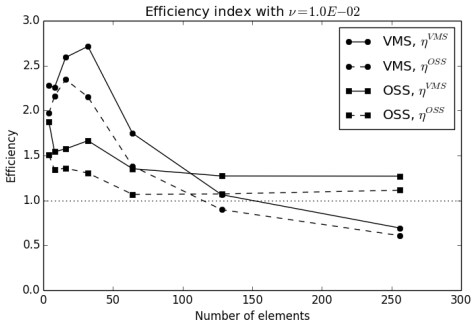

(b) $\nu = 1.0e-2$

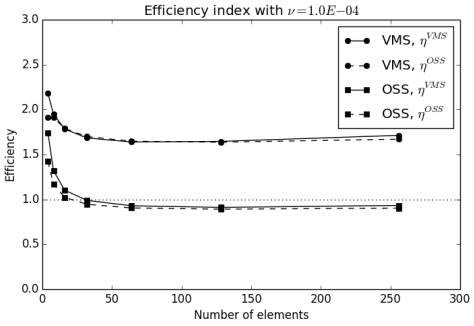

(c) $\nu = 1.0e-4$

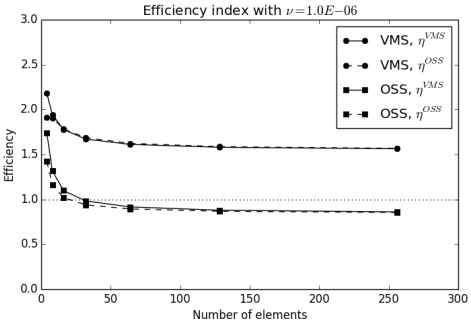

(d) $\nu = 1.0e-6$

Figure 3: *Problem A*. Global efficiency for different mesh sizes and viscosity values.

viscosity is reduced, the OSS method solution results in efficiencies closer to 1.0, while the VMS method gives higher efficiencies.

Remark. The cost of evaluation of the two error estimators, η^{OSS} and η^{VMS}, is identical, provided that the solution, u_h, and the orthogonal projection of the residual, $\Pi_h(f - \mathcal{L}u_h)$, are already computed. Note that when the standard VMS stabilization method is used to compute the solution, no projections are needed. Then, in order to evaluate η^{OSS}, we will have to perform an additional global solve to obtain the projections. Nevertheless, when the solution is computed using the OSS method, as we reuse the projections, no additional solve needs to be done to evaluate η^{OSS}. For this reason, the use of η^{OSS} is

more suitable when the OSS method is used as a stabilization method to compute the solution.

For the *boundary layer solution* test (problem B) stated in Section 4.1.2, we will only focus on the η^{VMS} error estimator evaluated on the VMS solution, and on the η^{OSS} estimator evaluated from the OSS solution. The global efficiency for the different viscosity and grid size values is shown in Figure 4. In that case the OSS approach results in efficiency values slightly larger than the standard VMS method, even for the advection-dominated cases. Note that for this test, the efficiency of the OSS error estimator is closer to 1.0, especially in Figure 4(c) and Figure 4(d).

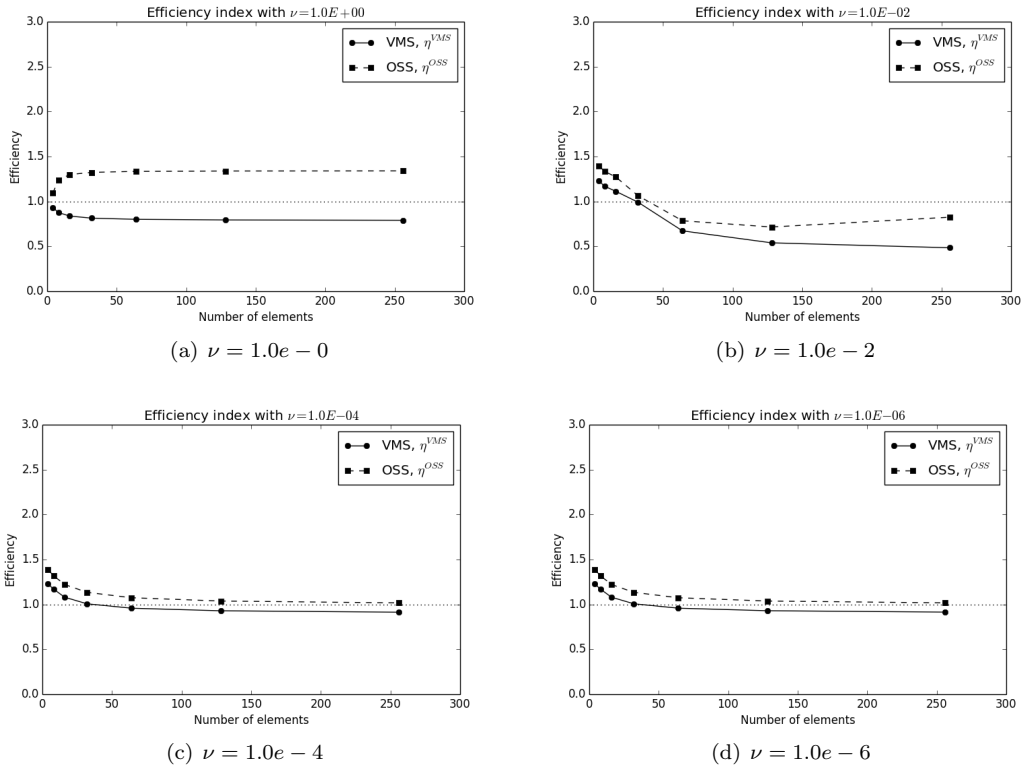

(a) $\nu = 1.0e-0$ (b) $\nu = 1.0e-2$

(c) $\nu = 1.0e-4$ (d) $\nu = 1.0e-6$

Figure 4: *Problem B.* Global efficiency for different mesh sizes and viscosity values.

In Figure 5 we depict the distribution of the local exact and estimated errors, Figure 5(a) and Figure 5(b), respectively, for a viscosity of $\nu = 1.0e-6$ using the OSS error estimator. Note that we have used the same logarithmic scale for both figures. The error estimator overpredicts the exact error in regions where the latter is close to zero, but matches it well in regions where the latter is large. Similar results were observed in [13].

Finally, we look at the results for the *sharp inner layer solution* (problem C). The global efficiency as a function of different viscosity values and grid sizes is shown in Figure 6. We can see that for this test, the efficiencies go to zero for both error estimators, see Figure 6(a)-Figure 6(c). However, when $\nu = 1.0e-6$, an efficiency of 1.0 is recovered, as shown in Figure 6(d).

To understand why the values of the efficiency index tend to zero for the viscous dominated cases, we look in more detail at the distribution of the local errors, depicted in Figure 7 for two different viscosity cases, $\nu = 1.0$ and $\nu = 1.0e-6$, in a 64^2 elements mesh. Note also that in such figures, the same logarithmic scales have been used for both the exact and estimated error plots. We can see that for $\nu = 1.0$, Figure 7(a) and Figure 7(b), the OSS error estimator underpredicts the exact error, especially at the corners. But the prediction is much more accurate for the case of $\nu = 1.0e-6$, Figure 7(c) and Figure 7(d), where the error estimator matches the exact error in terms of localization. It is important

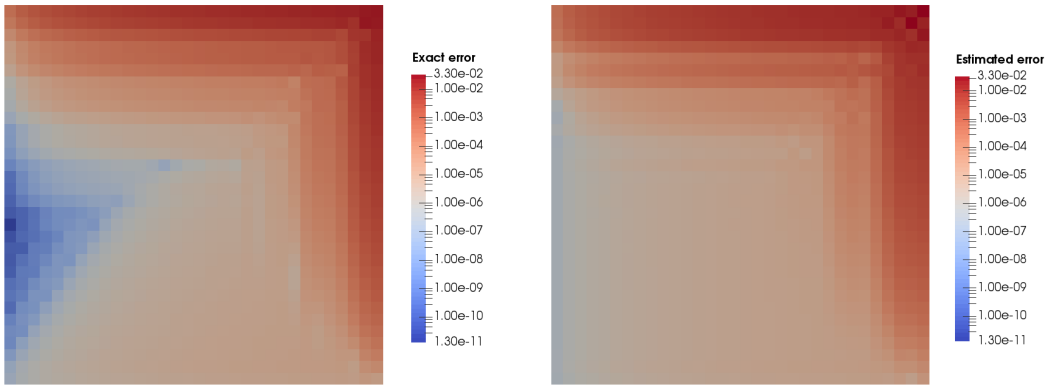

(a) Exact error. (b) Estimated error, η^{OSS}.

Figure 5: *Problem B.* Local exact and estimated errors with $\nu = 1.0e-6$.

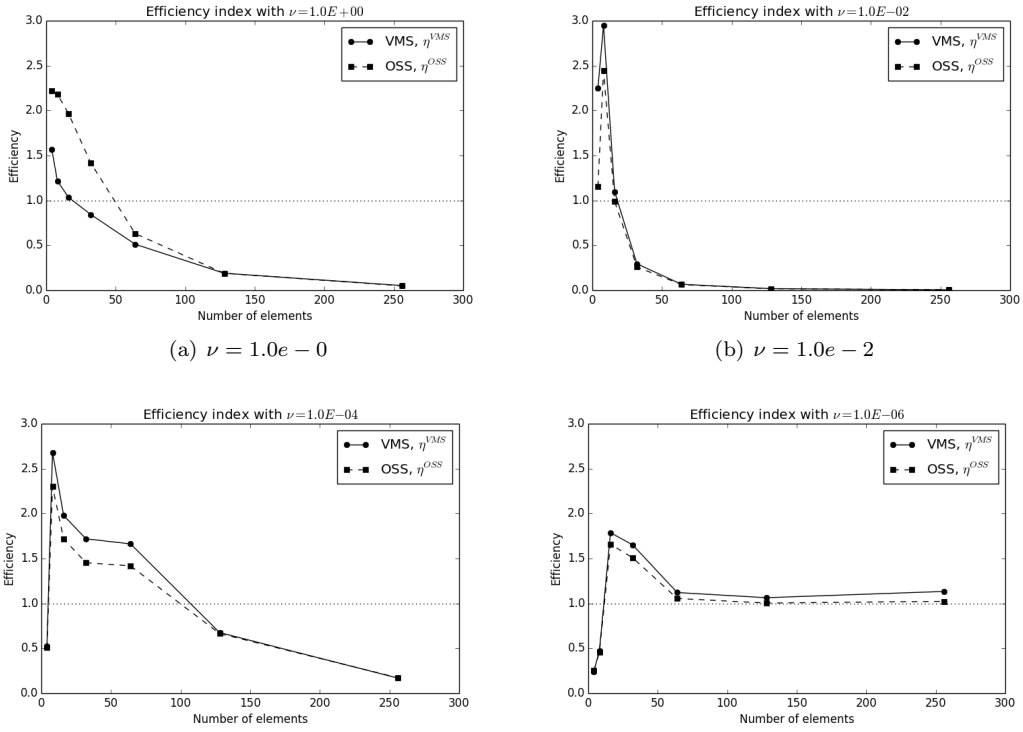

(a) $\nu = 1.0e-0$ (b) $\nu = 1.0e-2$

(c) $\nu = 1.0e-4$ (d) $\nu = 1.0e-6$

Figure 6: *Problem C.* Global efficiency for different mesh sizes and viscosity values.

to highlight that the values of the error for the first case, $\nu = 1.0$, are much lower than the case of $\nu = 1.0e-6$ (four orders of magnitude). This behavior indicates that the error estimator can predict the exact error location when this is relatively large, but it fails when the error is low ($\varepsilon_{\mathrm{num}} \sim 10^{-6}$).

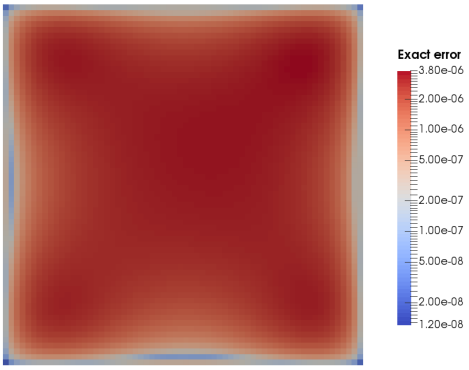

(a) Exact error with $\nu = 1.0$

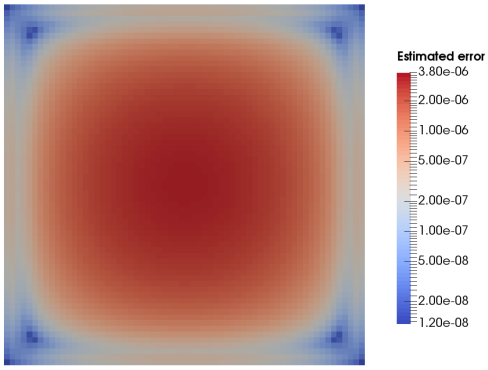

(b) Estimated error, η^{OSS}, with $\nu = 1.0$

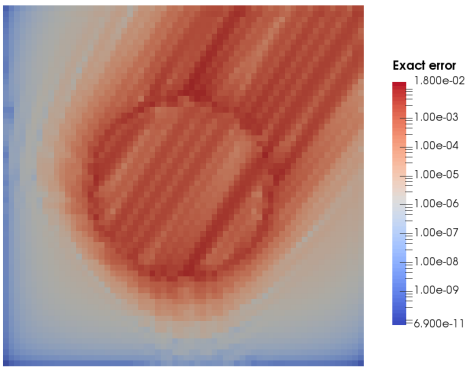

(c) Exact error with $\nu = 1.0e-6$

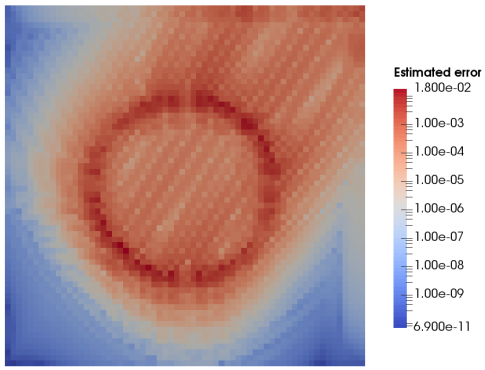

(d) Estimated error, η^{OSS}, with $\nu = 1.0e-6$

Figure 7: *Problem C.* Local exact and estimated errors with $\nu = 1.0$ and $\nu = 1.0e-6$.

4.2.1. Comparison with other error estimator definitions

The results of the previous section, can be put into perspective by comparing the performance of the OSS error estimator η^{OSS} with other errors estimators from the literature. In particular, we compare against the tests reported in [29], where six different error estimators are compared. Note that there is a slight difference with the reaction parameter value of problem A, which in this paper has been chosen $s = 1.0$, while in [29] is $s = 2.0$. A particular emphasis will be made to the error estimator denoted as η_{res-L^2}, which is a residual based error estimator in the L^2-norm, like the one proposed in this paper. We refer the reader to [29] for the exact definition of each estimator.

Figure 8 shows the values of the different error estimators for the three different problems of Section 4.1, for a viscosity value of $\nu = 1.0e-6$ in terms of the number of degrees of freedom (DOFs) used to solve the problem. As shown, the proposed error estimator performs well compared with the errors defined in [29]. In particular, the efficiencies of η^{OSS} are much closer to 1.0 than the equivalent η_{res-L^2}, demonstrating an improved robustness.

4.3. Parametric study

4.3.1. Effect of the mesh distortion

All the results shown in Section 4.2 have been computed on a uniform structured mesh with quadrilateral elements. Nevertheless, in practical situations the meshes in which one has to compute may not be structured neither uniform, and it is well known that the mesh configuration does have an effect on the final solution. A robust error estimator should be able to capture the increase of the numerical error

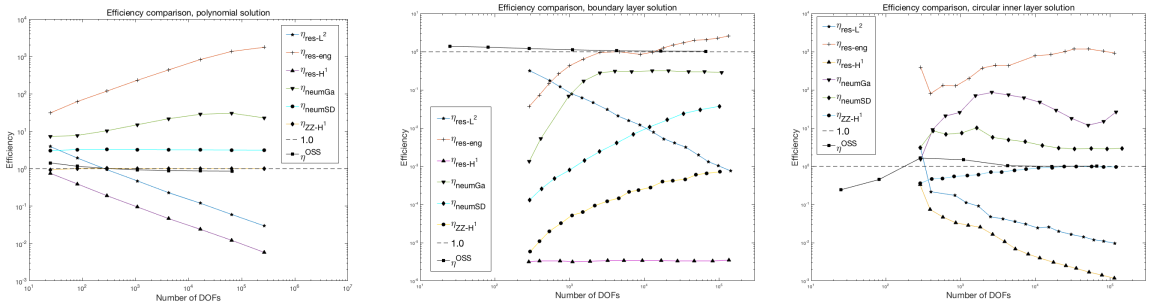

(a) *Problem A*, $\nu = 1.0e-6$ (b) *Problem B*, $\nu = 1.0e-6$ (c) *Problem C*, $\nu = 1.0e-6$

Figure 8: Comparison of the global efficiency between η^{OSS} and the results from [29].

when the mesh is distorted. In order to prove that the proposed error estimators are well-behaved when non-uniform meshes are used, we solve the problem on a distorted mesh whose coordinates have been modified according to the following law

$$\mathbf{x}_{\text{new}} = \mathbf{x}_{\text{old}} + \frac{1.0}{60.0} \prod_{i=1}^{d} \sin(2\pi\lambda x_{\text{old},i}), \tag{39}$$

with λ a parameter that controls the distortion of the mesh. In Figure 9(a) , Figure 9(b) and Figure 9(c) we plot the mesh when the mapping (39) is applied with $\lambda = 0.0$, $\lambda = 4.0$ and $\lambda = 8.0$, respectively. Note that for $\lambda > 8.0$, we would have non-convex elements.

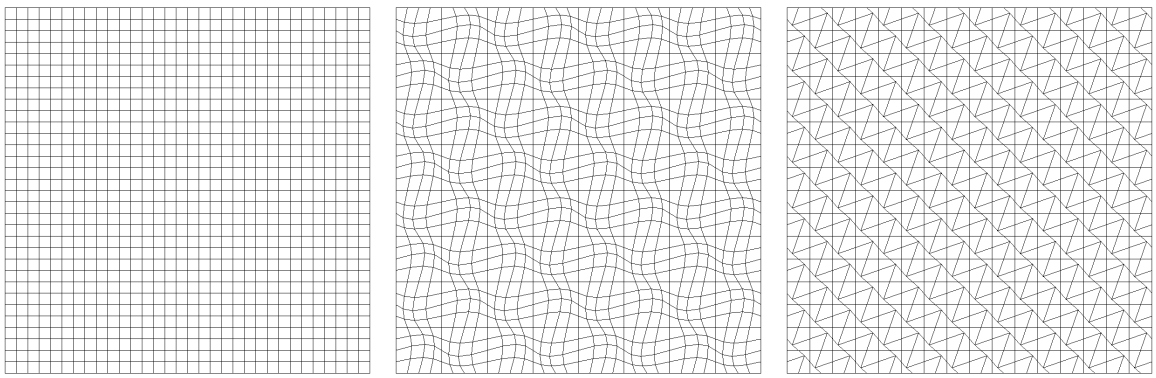

(a) $\lambda = 0.0$ (b) $\lambda = 4.0$ (c) $\lambda = 8.0$

Figure 9: Distorted meshes with 32^2 quadrilateral elements.

A parametric study is performed to check the behaviour of the error estimators with respect to the distortion of the mesh. The polynomial analytical solution test case (problem A) is solved using different meshes, with 32^2, 64^2 and 128^2 elements. A viscosity $\nu = 10^{-4}$ and an advection vector $\mathbf{a} = (3, 2)^T$ are taken. In Figure 10 we plot the evolution of the estimated error values, and the corresponding efficiencies, when the parameter λ varies from 0.0 to 8.0. As expected, we see that the estimated errors increase when the mesh is distorted (Figure 10(a), Figure 10(b) and Figure 10(c)). Note that for this case, both error estimators give very similar results, meaning that the mesh distortion is affecting the two error estimators in an analogous way.

Looking at Figure 10(d), Figure 10(e) and Figure 10(f)), we see that when the mesh is refined the efficiencies flatten, which can be interpreted as a reduction of the mesh distortion influence on the

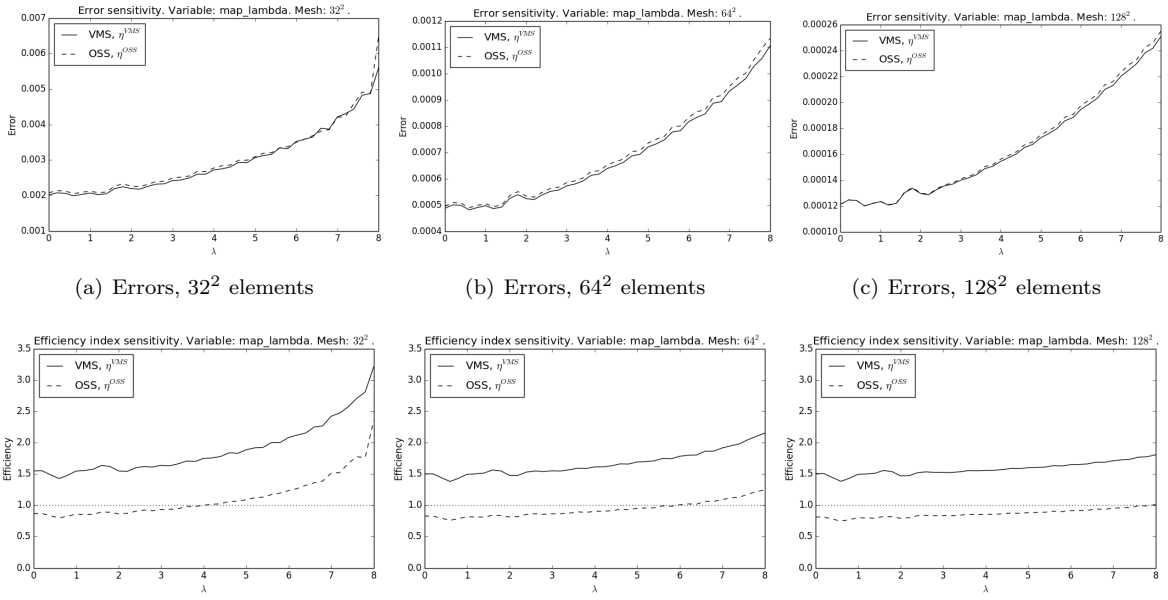

(a) Errors, 32^2 elements (b) Errors, 64^2 elements (c) Errors, 128^2 elements

(d) Efficiency, 32^2 elements (e) Efficiency, 64^2 elements (f) Efficiency, 128^2 elements

Figure 10: Evolution of the error and efficiency with respect to λ for different meshes.

accuracy of the error estimators. These results are also in concordance with Figure 3(c) (exactly the same for $\lambda = 0.0$), in which we have seen that the efficiency is higher for η^{VMS} and closer to 1.0 for η^{OSS}.

4.3.2. Effect of the viscosity

We have seen that the proposed error estimators have a good performance when refining the mesh for different viscosity values. But now we want to check in a more systematic way the sensitivity of the error estimators with respect to the physical parameters. In this subsection we perform a parametric study with respect to the viscosity.

An important goal of this analysis is to assess the smoothness of the error estimator as a function of the physical parameters. This will affect the performance of the propagation method used to account for uncertainty on the physical parameters, see Section 5.2.

In order to check the effect of the viscosity, we compute the error estimators for a given mesh size (32^2 and 64^2 elements mesh) for a viscosity $\nu \in [1.0e-6, 1.0]$. The global estimated error and efficiency results are plotted in Figure 11 for both definitions, η^{VMS} and η^{OSS}.

Looking at the estimated errors evolution shown in Figure 11(a) and Figure 11(c), we see that there are two clearly distinguishable regions: one in which the error estimators do not depend on the viscosity values, when $\nu < 1.0e-4$, and another region in which there is a high dependency on the viscosity, for $\nu > 1.0e-4$. We can identify these two regions as the advection dominated state and the viscous dominated state, respectively.

Note that the estimated errors present a cusp near $\nu = 1.0e-2$. This behaviour can be caused by the fact that we have an L^∞-norm on the definition of the error estimator, which can give this type of functions when the residual goes from positive to negative, or vice-versa. The efficiency plots, Figure 11(b) and Figure 11(d), inherit this cusp.

It is also noticeable that the OSS error estimator, η^{OSS}, gives efficiency values closer to 1.0 than the standard VMS error estimator, η^{VMS}.

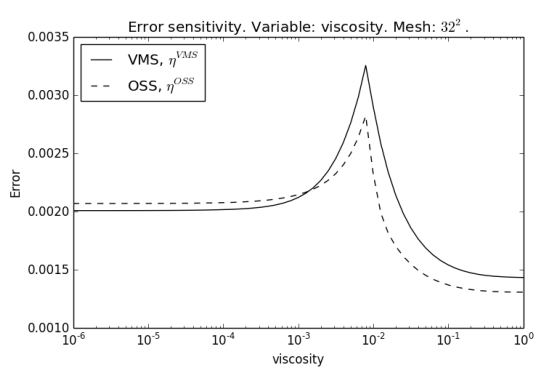

(a) Errors for a 32^2 elements mesh

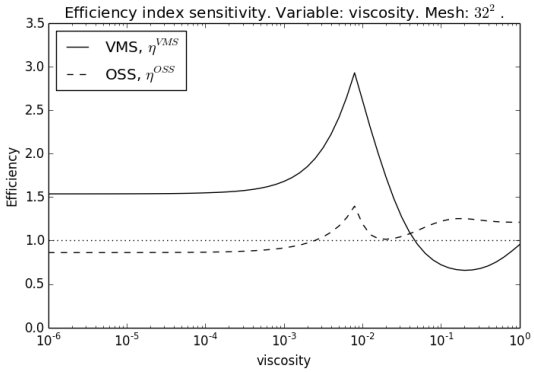

(b) Efficiency for a 32^2 elements mesh

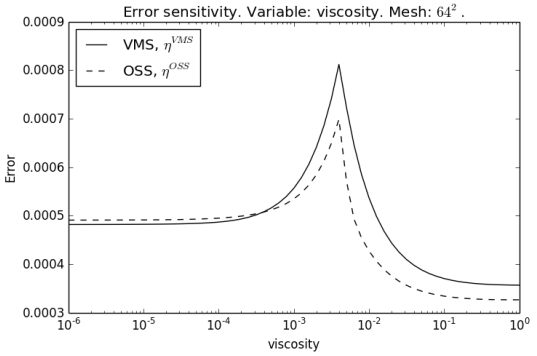

(c) Errors for a 64^2 elements mesh

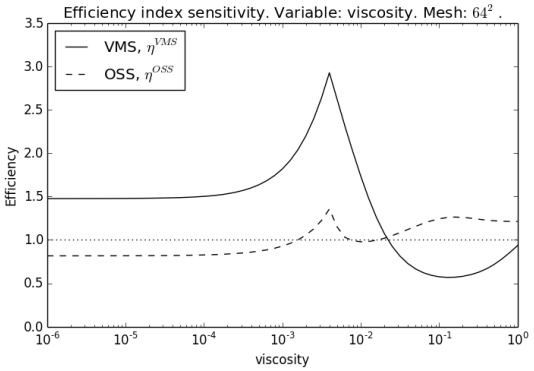

(d) Efficiency for a 64^2 elements mesh

Figure 11: *Polynomial solution*. Sensitivity analysis of the error estimators with respect to the viscosity.

4.3.3. Effect of the advection direction

The same analysis can be done varying the advection direction. In that case we select a direction in the range $\alpha \in [-\pi, \pi]$, keeping the advection magnitude constant $|\mathbf{a}| = \sqrt{3^2 + 2^2}$. We check the variation of the error estimators in the advection-dominated regime, with a viscosity $\nu = 1.0e-4$, and a reaction $s = 1.0$. The results for that case are shown in Figure 12, where a 64^2 elements mesh has been used.

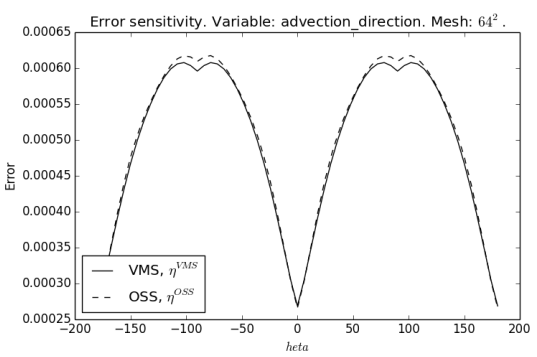

(a) Errors for a 64^2 elements mesh

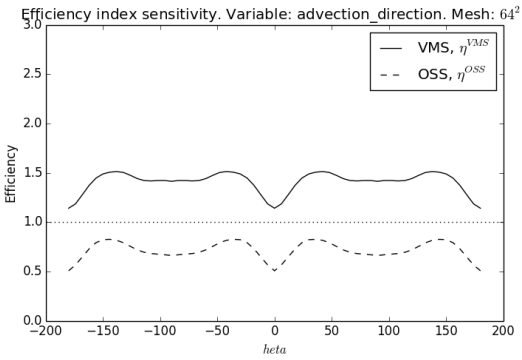

(b) Efficiency for a 64^2 elements mesh

Figure 12: *Polynomial solution*. Sensitivity analysis of the error estimators with respect to the advection direction.

In Figure 12(a) we see that the advection direction does affect the values of the error estimator, as expected. Nonetheless, the effect that this dependency has over the efficiency values is moderate, i.e. the accuracy of the error estimator is reasonably good for any advection direction angle. This is observed in Figure 12(b), where we see that the efficiency of η^{OSS} is kept between 0.5 and 1.0, and the efficiency of η^{VMS} between 1.0 and 1.5.

5. Uncertainty quantification

The aim of this section is to investigate the impact of system-parameter uncertainties on the error estimator. In turbulent flows, such uncertainties can be associated, for instance, with the unpredictability of the velocity fluctuations (in direction and/or magnitude) at a given time, see [30]. For this purpose, we first construct, in Section 5.1, probabilistic models for two physical input variables that critically impact the CDR solution, namely the viscosity ν and the advection direction α. These quantities are routinely assumed homogeneous over Ω (see e.g., [19, 21, 13]) and are thus modeled as random variables. We next address, in Section 5.2, the propagation of uncertainties using a standard stochastic collocation approach. Since the evolution of the two error estimators η^{VMS} and η^{OSS} with respect to the aforementioned problem parameters is similar (see Section 4.3), results are only reported for the OSS error estimator, η^{OSS}.

5.1. Construction of the probabilistic models

Let N and A be the random variables, defined on a probability space $(\Theta, \Sigma, \mathcal{P})$, with values in $\mathbb{R}_{>0}$ and $[-\pi, \pi]$ respectively, corresponding to the stochastic modeling of the viscosity ν and advection direction α. It is assumed below that N and A are statistically independent. Let H denote the random variable corresponding to the stochastic error estimator η^{OSS}. Let $L^2(\Theta, \mathbb{R})$ be the space of real-valued second-order random variables ($E\{X^2\} < +\infty$, $\forall\, X \in L^2(\Theta, \mathbb{R})$), equipped with the inner product

$$< X, Y >_\Theta = E\{XY\} = \int_\Theta X(\theta) Y(\theta)\, d\mathcal{P}(\theta) = \int_{\mathbb{R}} \int_{\mathbb{R}} xy\, P_{XY}(dx, dy) \ ,$$

where $P_{XY}(dx, dy)$ is the joint probability distribution of X and Y, and induced norm $\|X\|_\Theta = < X, X >_\Theta^{1/2}$, $L^2(\Theta, \mathbb{R})$ is a Hilbert space.

In order to account for the wide scale of variations in viscosity values, it is appropriate to introduce the Gaussian random variable X_ν with mean μ_{X_ν} and standard deviation σ_{X_ν}, defined in $(\Theta, \Sigma, \mathcal{P})$, with values in $\mathbb{R}$, such that

$$N = 10^{X_\nu}. \tag{40}$$

The probability density function p_N of N is thus given by

$$p_N(n) = \frac{1}{\sigma_{X_\nu} \ln(10) \sqrt{2\pi}} \times \frac{1}{n} \times \exp\left(- \left(\frac{\ln(n)/\ln(10) - \mu_{X_\nu}}{2\sigma_{X_\nu}} \right)^2 \right) \ , \quad \forall\, n > 0 \ . \tag{41}$$

The random variable X_ν is then expressed as

$$X_\nu = \mu_{X_\nu} + \sigma_{X_\nu} \Xi_1 \ , \tag{42}$$

where Ξ_1 is a standard Gaussian random variable.

The random variable A is next modeled through an affine transformation of an auxiliary Beta random variable:

$$A = -\pi + 2\pi B \ , \tag{43}$$

in which B follows a (unimodal) Beta distribution with shape parameters $\lambda_1 > 1$ and $\lambda_2 > 1$, $B \sim \mathcal{B}(\lambda_1, \lambda_2)$. Denoting by μ_A and σ_A^2 the mean and variance of A, respectively, it can de deduced that

$$\lambda_1 = -\frac{\pi \mu_A^2 + \pi \sigma_A^2 - \pi^3 + \phi(\mu_A, \sigma_A)}{2\pi \sigma_A^2} \tag{44}$$

and

$$\lambda_2 = -\frac{\pi\mu_A^2 + \pi\sigma_A^2 - \pi^3 - \phi(\mu_A, \sigma_A)}{2\pi\sigma_A^2} \ , \tag{45}$$

with

$$\phi(\mu_A, \sigma_A) = \mu_A(\mu_A^2 + \sigma_A^2 - \pi^2) \ . \tag{46}$$

Note that the conditions $\lambda_1 > 1$ and $\lambda_2 > 1$ yield implicit constraints on the admissible values of μ_A and σ_A. Denoting by $F_{\mathcal{B}(\lambda_1,\lambda_2)}$ and Φ the cumulative distribution functions of the Beta law $\mathcal{B}(\lambda_1, \lambda_2)$ and standard Gaussian law, respectively, it follows that

$$A = -\pi + 2\pi F^{-1}_{\mathcal{B}(\lambda_1,\lambda_2)}\left(\Phi(\Xi_2)\right) \ , \tag{47}$$

where Ξ_2 is a standard Gaussian random variable.

Note that the probabilistic models for N and A are constructed in such a way that: (i) they involve a low-dimensional parametrization, typically through mean and standard deviation values (the former being of primary importance to explore various regimes at the propagation stage); and (ii) they satisfy desired constraints, such as boundedness in the case of the random variable A. The aforementioned models then correspond to the probability distributions obtained by invoking the maximum entropy principle [31, 32, 33], which gives the most objective stochastic models that are consistent with the available information.

5.2. Framework for uncertainty propagation

Assuming that $H \in L^2(\Theta, \mathbb{R})$, an approximation of the solution map $H = \tilde{f}(N(\Xi_1), A(\Xi_2)) = f(\Xi_1, \Xi_2)$, where $\tilde{f}$ represents the action of the CDR operator (with physical variables), is then classically constructed using a polynomial chaos expansion (PCE) with a Gaussian germ, [34, 35, 36, 37].

$$H = \sum_{\boldsymbol{\beta}, |\boldsymbol{\beta}|=0}^{+\infty} h_{\boldsymbol{\beta}} \Psi_{\boldsymbol{\beta}}(\boldsymbol{\Xi}) \tag{48}$$

where $\boldsymbol{\beta} = (\beta_1, \beta_2) \in \mathbb{N}^2$ is a multi-index with $|\boldsymbol{\beta}| = \beta_1 + \beta_2$, $\{\Psi_{\boldsymbol{\beta}}\}_{\boldsymbol{\beta}}$ are the (normalized) multi-dimensional Hermite polynomials and $\boldsymbol{\Xi} = (\Xi_1, \Xi_2)$. These polynomials form an orthonormal basis with respect to the standard Gaussian measure $P_{\boldsymbol{\Xi}}(d\boldsymbol{\xi}) = p_{\boldsymbol{\Xi}}(\boldsymbol{\xi})d\boldsymbol{\xi}$ on $\mathbb{R}^2$:

$$< \Psi_{\boldsymbol{\beta}}, \Psi_{\boldsymbol{\beta}'} >_\Theta = \int_{\mathbb{R}^2} \Psi_{\boldsymbol{\beta}}(\boldsymbol{\xi})\Psi_{\boldsymbol{\beta}'}(\boldsymbol{\xi})\, p_{\boldsymbol{\Xi}}(\boldsymbol{\xi}) d\boldsymbol{\xi} = \prod_{i=1}^{2} \delta_{\beta_i \beta'_i} \ , \tag{49}$$

with δ_{ij} the Kronecker delta. As a consequence, one has

$$h_{\boldsymbol{\beta}} =< H, \Psi_{\boldsymbol{\beta}} >_\Theta \ . \tag{50}$$

In practice, a mean-square convergent truncated series is considered:

$$H^{(Q)} = \sum_{\boldsymbol{\beta}, |\boldsymbol{\beta}|=0}^{Q} h_{\boldsymbol{\beta}} \Psi_{\boldsymbol{\beta}}(\boldsymbol{\Xi}) \ . \tag{51}$$

Let $N_{pce} = (2+Q)!/(2Q!)$ be number of terms contained in the above series. Assuming a lexicographical ordering of the multi-indices, Eq. (51) can be conveniently rewritten (with obvious notations) as

$$H^{(N_{pce})} = \sum_{i=0}^{N_{pce}-1} h_i \Psi_i(\boldsymbol{\Xi}) \ . \tag{52}$$

Note that some applications below involve one single random variable (i.e. either Ξ_1 or Ξ_2, for problems where only the viscosity or the advection direction is randomized, respectively), in which case the above

classical formulation reduces in a straightforward manner. Various methods have been proposed in the literature to evaluate the chaos coefficients in Eq. (50), see e.g.,[2, 38, 39]. In what follows, a Gauss-Legendre or Genz-Keister nested rules were used for low stochastic dimensions, and the sparse pseudospectral approach developed in [40] was used for higher orders. All computations have been conducted using DAKOTA (see [41]), interfaced with FEMPAR.

5.3. Numerical results for problem A and B with random viscosity

Throughout this section, uncertainty propagation is achieved considering the stochastic viscosity exponent X_ν as the sole random input (defined in Section 5.1), the advection direction being set to $\mathbf{a} = (3, 2)^T$. The manufactured polynomial and boundary layers solutions described in Section 4.1.1 and Section 4.1.2 are used as benchmark problems. Based on the results shown in Figure 11(a), two mean values of X_ν are purposely selected to address smooth and non-smooth regimes: the latter will correspond to $\mu_{X_\nu} = -4.0$ and $\mu_{X_\nu} = -2.2$, respectively.

5.3.1. Convergence analysis of the PCE

In this section, the convergence of the PCE is assessed for a uniform mesh of 32^2 quadrilateral elements. The Monte Carlo method is used as the reference stochastic solver, considering $M = 10^5$ independent realizations of the input random variable. In what follows, this reference solution is denoted with the superscript "0". The convergence study is carried out by taking $N_{pce} = \{2, 4, 8, 32, 64, 128\}$, and the numerical integration is done with at least $n_{qp} = N_{pce} + 1$ quadrature points. The error function $N_{pce} \mapsto e_\Theta(N_{pce})$ is defined as

$$e_\Theta(N_{pce}) = \|H^{(N_{pce})} - H^0\|_\Theta \ .$$

The convergence of this error function can be observed in Figure 13 for both $\mu_{X_\nu} = -4.0$ and $\mu_{X_\nu} = -2.2$. In the former case, the PCE exhibits fast convergence, with results close to the reference solution

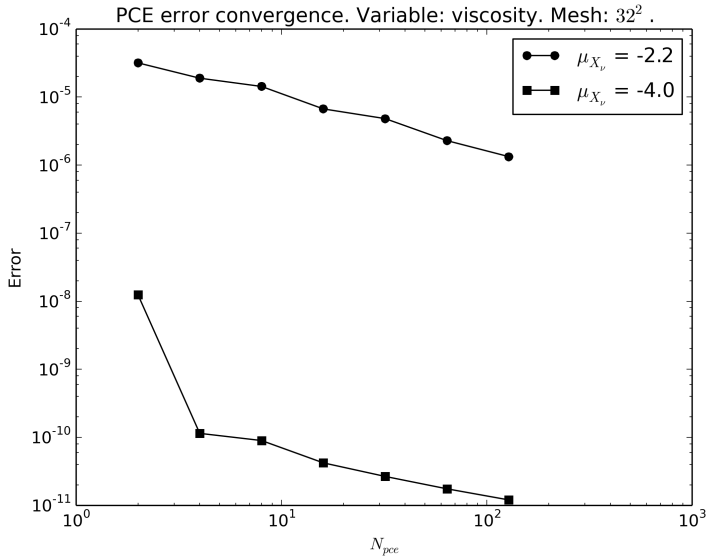

Figure 13: *Problem A*. Convergence of the L^2-norm of the error, e_Θ, for the case $\mu_{X_\nu} = -4.0$ and $\mu_{X_\nu} = -2.2$.

even at small orders ($N_{pce} = 2$ or 4). This is an expected behavior, as the solution map is smooth in the explored viscosity regime (convection-dominated regime; see Figure 11(a)) and can thus be described with the global basis functions. In contrast, the L^2 errors obtained with the second case, $\mu_{X_\nu} = -2.2$, are much larger, and high orders are required to reach a reasonable approximation. This result is induced by the non-smoothness of the solution in the viscous-dominated regime (see Section 4.3.2), which challenges

the PCE. These behaviors are illustrated in Figure 14, in which the values of the OSS error estimator are reported for a set of 12,800 samples, as well as in Figure 15, where results are shown using probability density functions. For non-smooth response functions, potential remedies include the use of local basis functions [42] or spectral products (see [38, Chapter 4.5.4]). Investigating such methods is out of the scope of the current work and will be considered in future works.

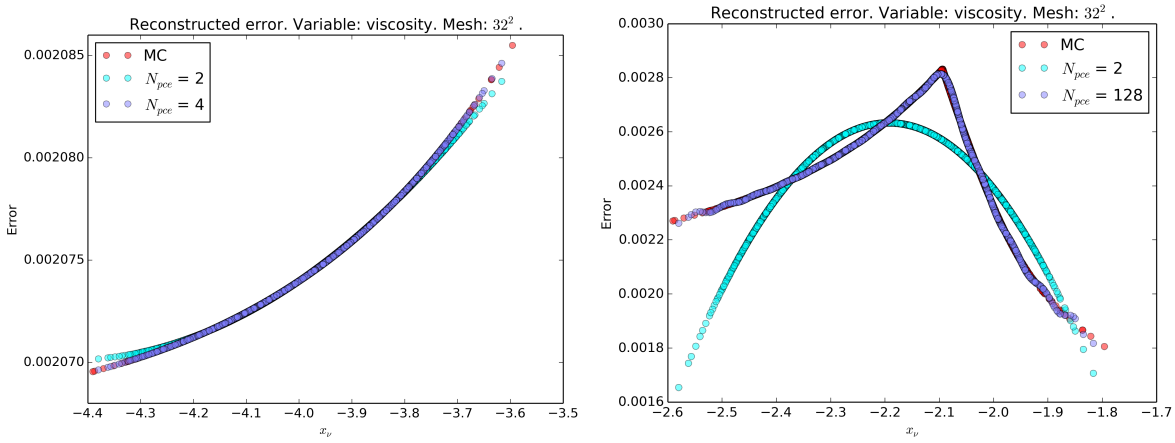

(a) $\mu_{X_\nu} = -4.0$. (b) $\mu_{X_\nu} = -2.2$.

Figure 14: *Problem A*. Realizations of a 12800 samples set for the MC and PCE methods with different number of quadrature points.

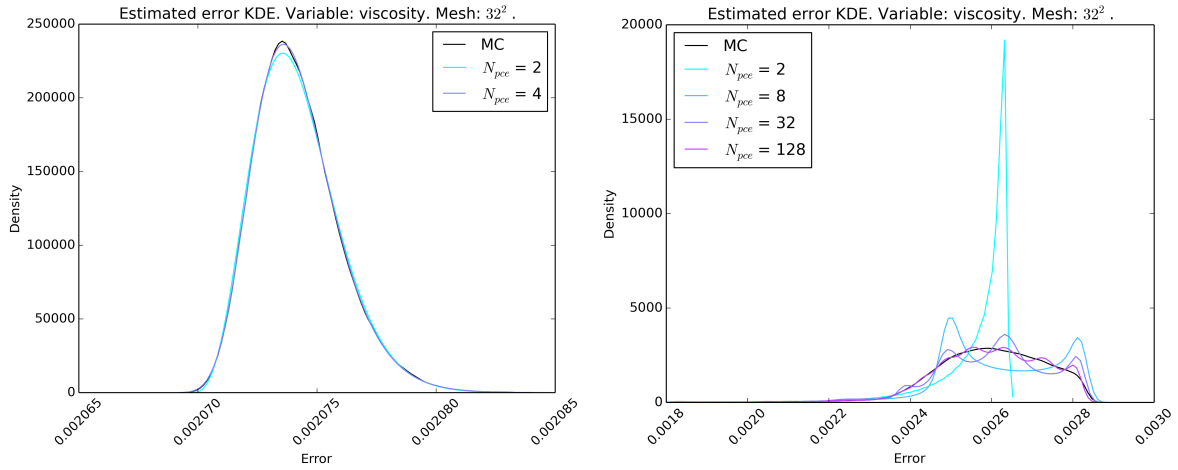

(a) $\mu_{X_\nu} = -4.0$. (b) $\mu_{X_\nu} = -2.2$.

Figure 15: *Problem A*. Estimated error KDE ($\hat{p}_\eta(\eta)$) using the PCE method for the case $\mu_{X_\nu} = -4.0$ (left) and $\mu_{X_\nu} = -2.2$ (right).

Remark. The poor convergence of the PCE is expected for functions of the absolute value type, which is the case of the error estimator η^{OSS} under consideration (see (32), and note the presence of the L^∞-norm).

5.3.2. Comparison between the stochastic exact and estimated errors in a parameter independent solution

This section is dedicated to the comparison between the stochastic exact error, denoted as $\mathcal{E}^{(N_{pce})}$, and the stochastic estimated error, $H^{(N_{pce})}$. Note that $\mathcal{E}^{(N_{pce})}$ is a random variable corresponding to the exact error, approximated using a PCE approach equivalent to (52),

$$\mathcal{E}^{(N_{pce})} = \sum_{i=0}^{N_{pce}-1} e_i \Psi_i(\boldsymbol{\Xi}) \ . \tag{53}$$

with the coefficients, e_i, computed using a quadrature rule in which each quadrature point evaluation is obtained analytically from the solution (36). In order to perform the analysis, three mean values for the random exponent are considered, $\mu_{X_\nu} = \{-6, -4, -2\}$. The last two values correspond to the cases addressed in the previous section, while $\mu_{X_\nu} = -6$ is considered to explore the asymptotic convection regime. A standard deviation of $\sigma_{X_\nu} = 0.1$ is selected for all cases, and a fixed advection direction, defined by $\alpha_{\mathbf{a}} = 33.69°$, is used. Here, the computation of the chaos coefficients is done using the Genz-Keister nested quadrature rule (in which the tolerance on the 2-norm of the change in the response covariance matrix is set to $1.0e-4$, hence yielding a maximum of 4 refinement iterations).

The histograms and the KDE for the exact error distribution and the OSS error estimator distribution are reported in Figure 16. Three different structured meshes are considered, consisting of 32^2, 64^2 and 128^2 quadrilateral elements (from left to right). For $\mu_{X_\nu} = -2.0$ (see the top row in Figure 16), the results show that the stochasticity in the viscosity generates high fluctuations for both the exact and estimated errors. This behavior is expected since this mean value corresponds to a viscous dominated regime, as shown in Section 4.3. For $\mu_{X_\nu} = -4.0$ (middle row), the level of statistical fluctuations significantly decreases, in accordance with the sensitivity analysis shown in Figure 11. A more extreme behavior is observed for $\mu_{X_\nu} = -6.0$ (bottom row), for which the estimated and exact errors are almost deterministic. Finally, it should be noticed that the evolution of the mean behavior while refining the mesh is consistent with standard results obtained within deterministic settings, for the three configurations tested.

In order to provide a quantitative insight in the comparison of the probability density functions in Figure 16, we present, in Table 1, the coefficients of variation of both, the exact and estimated error distributions, for different meshes and viscosity values. As expected, the coefficient of variation decreases

Table 1: Coefficient of variation of the distributions shown in Figure 16.

Elements	$\mu_{X_\nu} = -2.0$		$\mu_{X_\nu} = -4.0$		$\mu_{X_\nu} = -6.0$	
	Exact	η^{OSS}	Exact	η^{OSS}	Exact	η^{OSS}
32^2	$4.07e-02$	$1.33e-01$	$5.91e-04$	$8.64e-04$	$5.93e-06$	$8.64e-06$
64^2	$5.12e-02$	$6.20e-02$	$1.05e-03$	$2.00e-03$	$1.06e-05$	$2.00e-05$
128^2	$5.13e-02$	$3.28e-02$	$1.96e-03$	$4.42e-03$	$1.99e-05$	$4.30e-05$

when the problem becomes convection-dominated (results from left to right in Table 1), while the effect of mesh refinement is less pronounced (from top row to bottom row). In addition, the values for the exact and estimated errors are found to be of the same order.

5.3.3. Comparison between the stochastic exact and estimated errors in a parameter dependent solution

In Section 5.3.2 we have compared the exact and estimated errors for the test problem A, whose analytical solution is independent of the uncertain parameters. In order to deepen the analysis, in this section we compare the errors for problem B (see (37)), in which the analytical solution depends on the uncertain viscosity. The same three mean values for the random exponent are considered, $\mu_{X_\nu} = \{-6.0, -4.0, -2.0\}$, and the same standard deviation of $\sigma_{X_\nu} = 0.1$ is selected for all cases. Likewise the advection direction is fixed with a direction defined by $\alpha_{\mathbf{a}} = 56.31°$. The same setting for the polynomial chaos coefficients computations as in Section 5.3.2 is considered here.

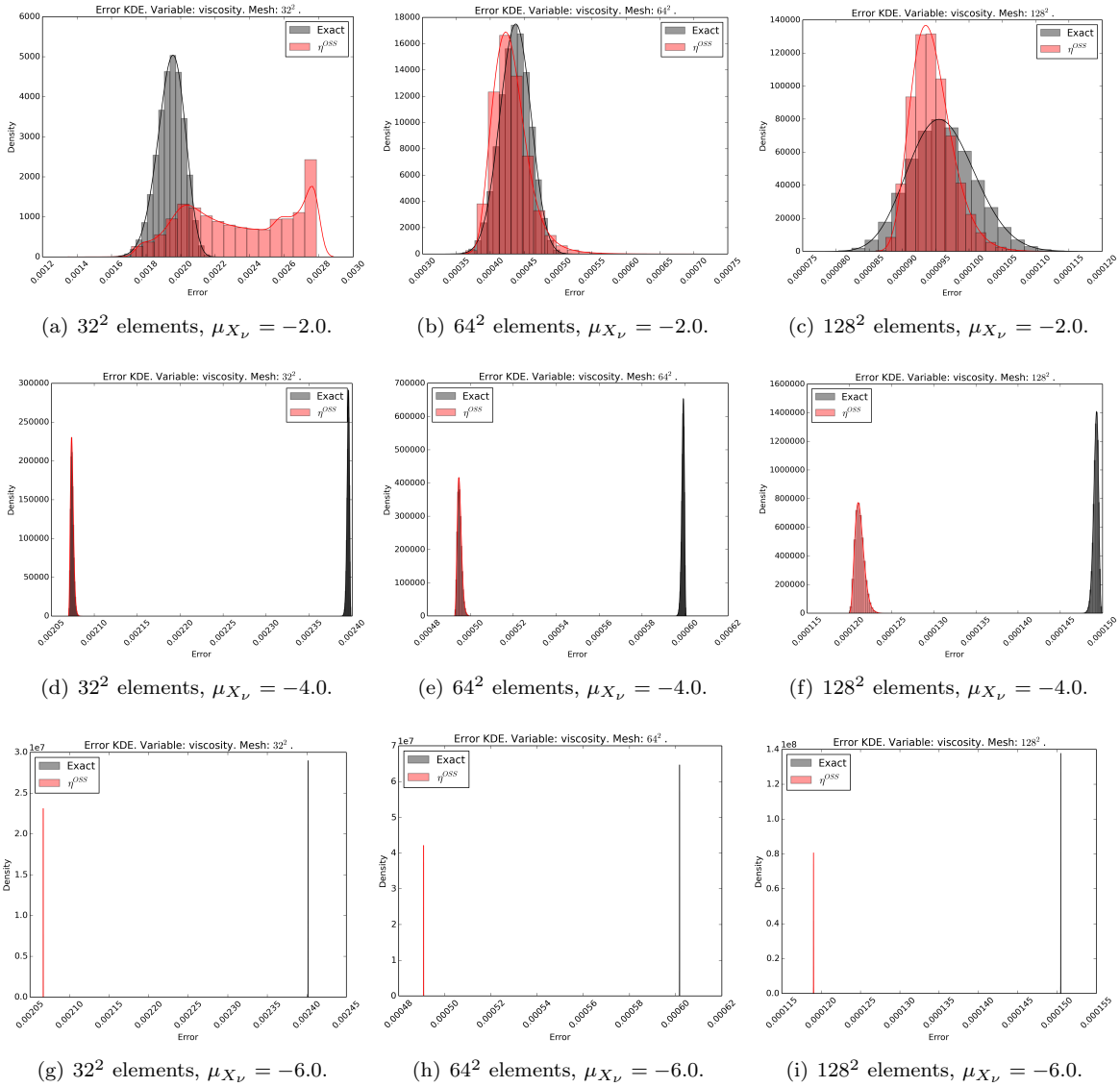

(a) 32^2 elements, $\mu_{X_\nu} = -2.0$. (b) 64^2 elements, $\mu_{X_\nu} = -2.0$. (c) 128^2 elements, $\mu_{X_\nu} = -2.0$.

(d) 32^2 elements, $\mu_{X_\nu} = -4.0$. (e) 64^2 elements, $\mu_{X_\nu} = -4.0$. (f) 128^2 elements, $\mu_{X_\nu} = -4.0$.

(g) 32^2 elements, $\mu_{X_\nu} = -6.0$. (h) 64^2 elements, $\mu_{X_\nu} = -6.0$. (i) 128^2 elements, $\mu_{X_\nu} = -6.0$.

Figure 16: *Problem A*. Histogram and KDE for different meshes (32^2, 64^2 and 128^2 elements) and different viscosity values ($\mu_{X_\nu} = -2.0$, $\mu_{X_\nu} = -4.0$ and $\mu_{X_\nu} = -6.0$). The resulting expansion orders for each subfigure are the following: (a) $N_{pce} = 14$, (b-c) $N_{pce} = 7$, (d-i) $N_{pce} = 2$.

Figure 17 depicts the histograms and the KDE for the exact error distribution and the OSS error estimator distribution. Again, three different structured meshes are considered, consisting of 32^2, 64^2 and 128^2 quadrilateral elements (from left to right). Comparing Figure 16 and Figure 17 we see that similar results are observed for both problems. As in the previous section, for $\mu_{X_\nu} = -2.0$ (see the top row in Figure 17), we see that the stochastic viscosity results in high fluctuations for both the exact and estimated errors. Similarly, for $\mu_{X_\nu} = -4.0$ (middle row), the level of statistical fluctuations significantly decreases, and for $\mu_{X_\nu} = -6.0$ (bottom row) the estimated and exact errors are almost deterministic. Note that, unlike the results shown in Figure 16, the error is overestimated for problem B.

In Table 2, we show the coefficients of variation of both the exact and estimated error distributions, for different meshes and viscosity values. The same general conclusions can be drown from Table 1 and Table 2, where the reduction of the viscosity towards the convection-dominated (see the results

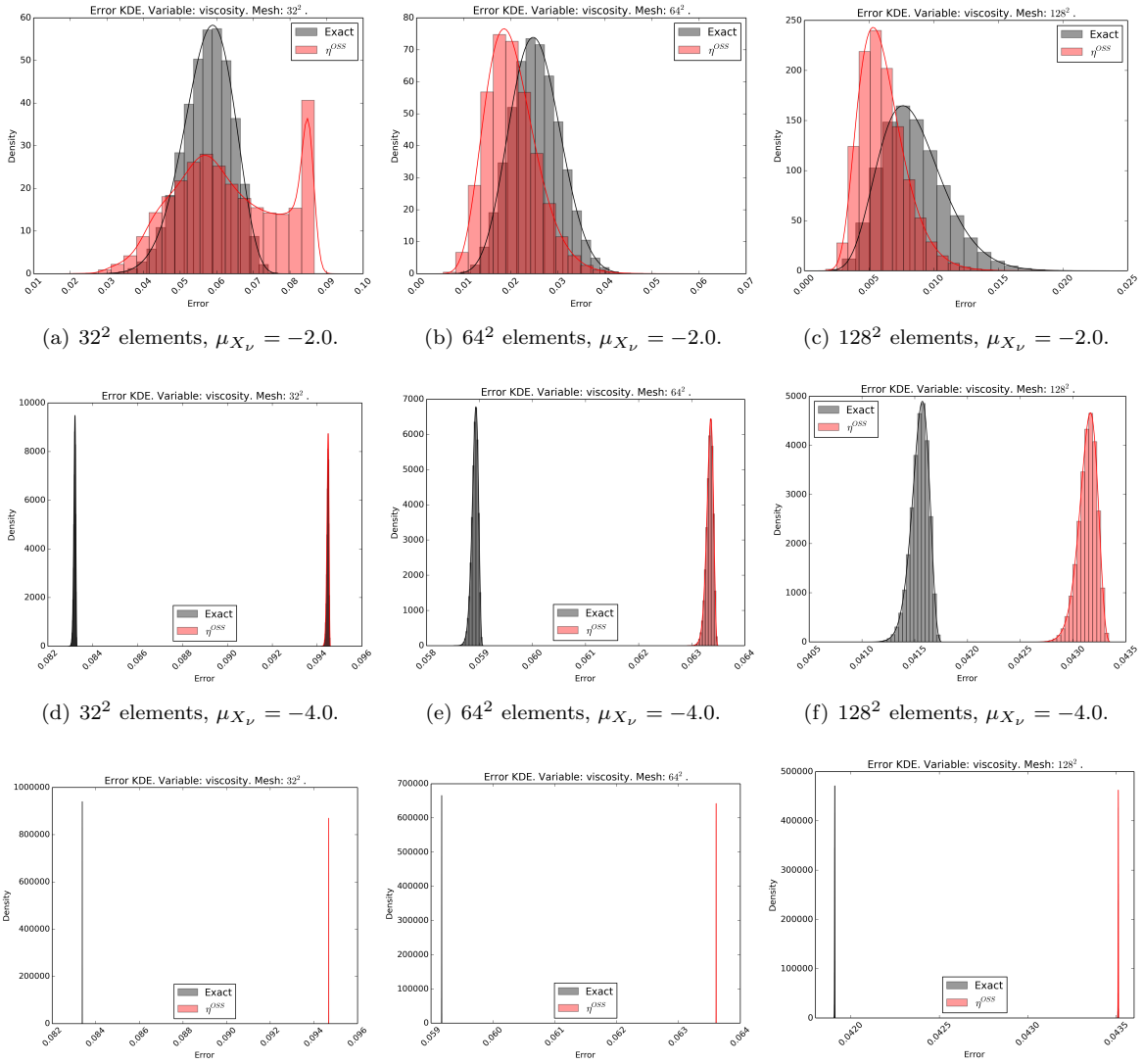

(a) 32^2 elements, $\mu_{X_\nu} = -2.0$. (b) 64^2 elements, $\mu_{X_\nu} = -2.0$. (c) 128^2 elements, $\mu_{X_\nu} = -2.0$.

(d) 32^2 elements, $\mu_{X_\nu} = -4.0$. (e) 64^2 elements, $\mu_{X_\nu} = -4.0$. (f) 128^2 elements, $\mu_{X_\nu} = -4.0$.

(g) 32^2 elements, $\mu_{X_\nu} = -6.0$. (h) 64^2 elements, $\mu_{X_\nu} = -6.0$. (i) 128^2 elements, $\mu_{X_\nu} = -6.0$.

Figure 17: *Problem B.* Histogram and KDE for different meshes (32^2, 64^2 and 128^2 elements) and different viscosity values ($\mu_{X_\nu} = -2.0$, $\mu_{X_\nu} = -4.0$ and $\mu_{X_\nu} = -6.0$). The resulting expansion orders for each subfigure are the following: (a) $N_{pce} = 25$, (b-c) $N_{pce} = 7$, (d-i) $N_{pce} = 2$.

Table 2: Coefficient of variation of the distributions shown in Figure 17.

Elements	$\mu_{X_\nu} = -2.0$		$\mu_{X_\nu} = -4.0$		$\mu_{X_\nu} = -6.0$	
	Exact	η^{OSS}	Exact	η^{OSS}	Exact	η^{OSS}
32^2	$1.17e-01$	$2.27e-01$	$5.22e-04$	$4.99e-04$	$5.27e-06$	$5.01e-06$
64^2	$2.08e-01$	$2.68e-01$	$1.03e-03$	$1.01e-03$	$1.05e-05$	$1.01e-05$
128^2	$2.96e-01$	$2.94e-01$	$2.02e-03$	$2.05e-03$	$2.09e-05$	$2.05e-05$

from left to right) is the dominant factor affecting the coefficient of variation. Instead, the effect of mesh refinement is less important (see the results from top to bottom row). Note that in problem B,

the values of the coefficient of variation for the exact and estimated error distributions are in better agreement than in problem A.

5.4. Numerical results for problem A with random advection direction

In this section, uncertainty propagation is investigated on the manufactured solution problem A, parametrized by a deterministic viscosities (with values coinciding to the mean models introduced in the previous section, $\nu = \{10^{-2.0}, 10^{-4.0}, 10^{-6.0}\}$) and a stochastic advection direction A (defined in Section 5.1). The mean value of the latter is set to $\mu_A = 33.69°$, and a standard deviation of $\sigma_A = 5°$ is used. Note that for each setting, the convergence of the PCE is ensured.

The results are shown in Figure 18 for the three different meshes introduced previously. For low

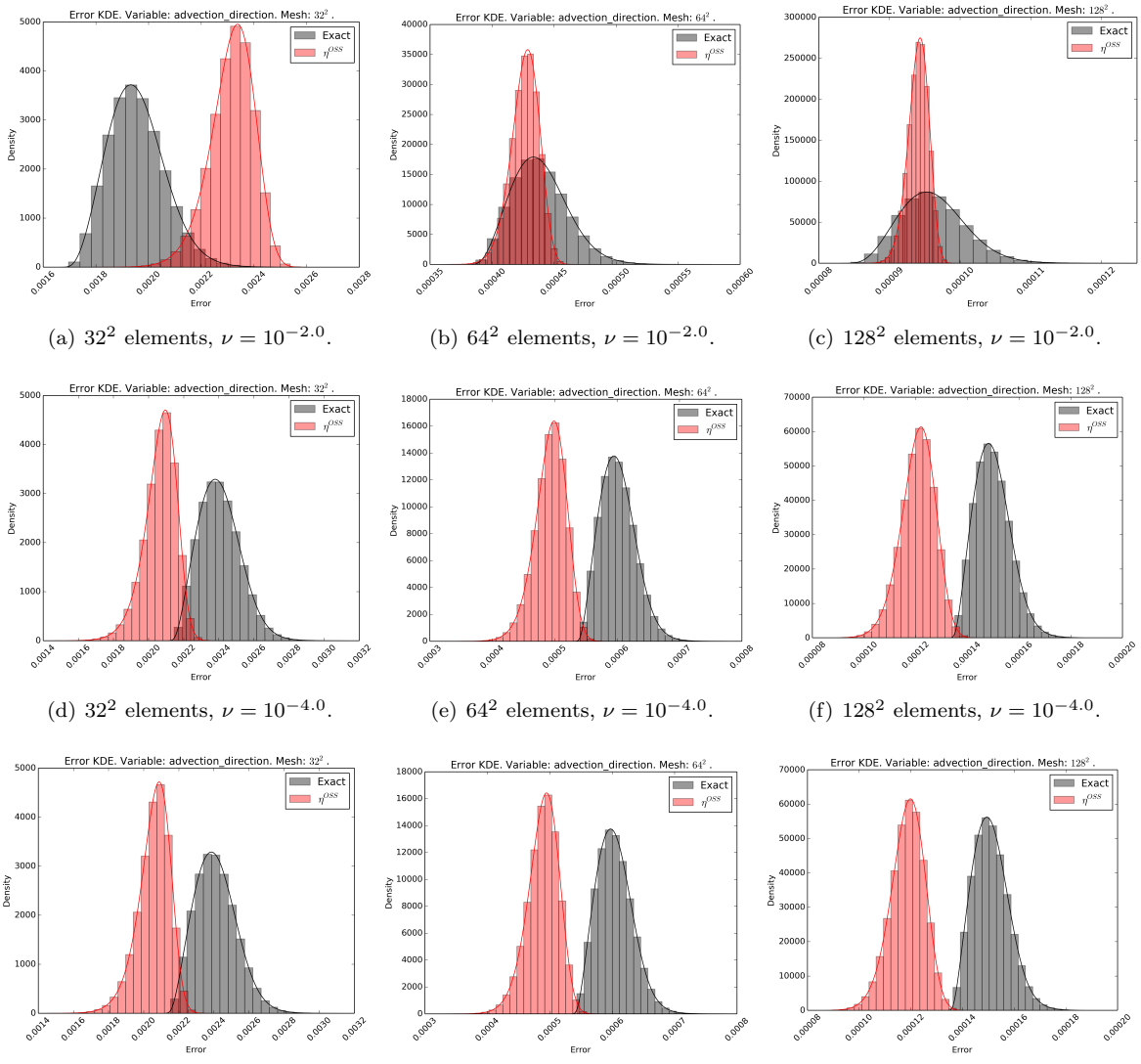

(a) 32^2 elements, $\nu = 10^{-2.0}$. (b) 64^2 elements, $\nu = 10^{-2.0}$. (c) 128^2 elements, $\nu = 10^{-2.0}$.

(d) 32^2 elements, $\nu = 10^{-4.0}$. (e) 64^2 elements, $\nu = 10^{-4.0}$. (f) 128^2 elements, $\nu = 10^{-4.0}$.

(g) 32^2 elements, $\nu = 10^{-6.0}$. (h) 64^2 elements, $\nu = 10^{-6.0}$. (i) 128^2 elements, $\nu = 10^{-6.0}$.

Figure 18: *Problem A*. KDE for different samples set for the MC method (top) and for different collocation points for the SC method (bottom). The resulting expansion orders for each subfigure are the following: (a-c) $N_{pce} = 7$, (d-i) $N_{pce} = 14$.

viscosity values (top row), the spread of the estimated error distribution gets smaller than the spread of the exact error distribution as the mesh is refined. Although this case is viscous dominated, it is

seen that the variation of the advection direction also has an impact on the estimated and exact errors. Similar results are obtained for $\nu = 10^{-4.0}$ (middle row) and $\nu = 10^{-6.0}$ (bottom row). These two cases are in the advection dominated regime, and we see that the effect of a varying advection direction is the same for both viscosity values.

The values of the coefficients of variation associated with the probability density functions depicted in Figure 18 are reported in Table 3. These coefficients are of the same order for the three viscosity cases considered. As noticed before, these results show that the variability on the advection direction produce variation on the error (estimated and exact), irrespective of the Péclet number.

Table 3: Coefficient of variation of the distributions shown in Figure 18.

Elements	$\nu = 10^{-2.0}$		$\nu = 10^{-4.0}$		$\nu = 10^{-6.0}$	
	Exact	η^{OSS}	Exact	η^{OSS}	Exact	η^{OSS}
32^2	$5.41e-02$	$3.62e-02$	$4.88e-02$	$4.45e-02$	$4.87e-02$	$4.45e-02$
64^2	$5.04e-02$	$2.64e-02$	$4.68e-02$	$5.10e-02$	$4.67e-02$	$5.12e-02$
128^2	$4.74e-02$	$1.55e-02$	$4.58e-02$	$5.45e-02$	$4.57e-02$	$5.53e-02$

5.5. Characterization of the stochastic efficiency index for problems A, B and C

In a deterministic setup, the difference between the estimated and the exact errors can be measured by the efficiency index defined in (35). It is then natural, within this uncertainty propagation analysis, to introduce its random version, denoted by $\mathcal{I}_{\text{eff}}$. This random variable, defined on $(\Theta, \Sigma, \mathcal{P})$, is then defined as

$$\mathcal{I}_{\text{eff}} = \frac{H}{\mathcal{E}} \ ,$$

where $\mathcal{E}$ is the random variable corresponding to the stochastic exact error. Below, the characterization of $\mathcal{I}_{\text{eff}}$ is performed for the three manufactured solution problems, and three probabilistic setups are examined:

- in the first case (C1), the setup coincides with the one introduced in Section 5.3, meaning that only the viscosity parameter is randomized (the mean values and standard deviation remain the same);
- the second case (C2) corresponds to the parametrization detailed in Section 5.4, involving the stochastic advection direction (here again, the values of the hyper-parameters are preserved);
- in the third configuration (C3), both the viscosity and advection direction are made stochastic.

In all cases, convergence analysis for the PCE are carried out following the strategy detailed in the previous sections. The results characterizing $\mathcal{I}_{\text{eff}}$ for the polynomial manufactured solution (36) (problem A) are shown in Figure 19. The case of a random viscosity and a fixed advection direction (case (C1)) is shown in the top row. As shown previously, the variability on the viscosity does not affect the efficiency index for the case $X_\nu = -6.0$ (right panel), which is convection dominated. In this case, the efficiency index tends to become deterministic. Of course, the impact of the stochasticity in the viscosity parameter increases while transitioning toward the viscous dominated regime. For $X_\nu = -4.0$ (middle panel), the efficiency index varies less for coarse meshes than for fine meshes, although the variation remains contained overall. This behavior is reversed for $X_\nu = -2.0$ (left panel), where the coarsest meshes have a distribution with values between 1.0 and 1.45, while the finest meshes have a distribution with efficiency values between 0.95 and 1.05.

When only the advection direction is randomized (case (C2)), the efficiency index presents substantial variability for the three values of the deterministic viscosity (middle row). When $\nu = 1.0e-4$ (middle panel) and $\nu = 1.0e-6$ (right panel), the distributions of the efficiency index are very similar. That is an expected result, since for these two cases, the flow is convection dominated. Moreover, we see that for

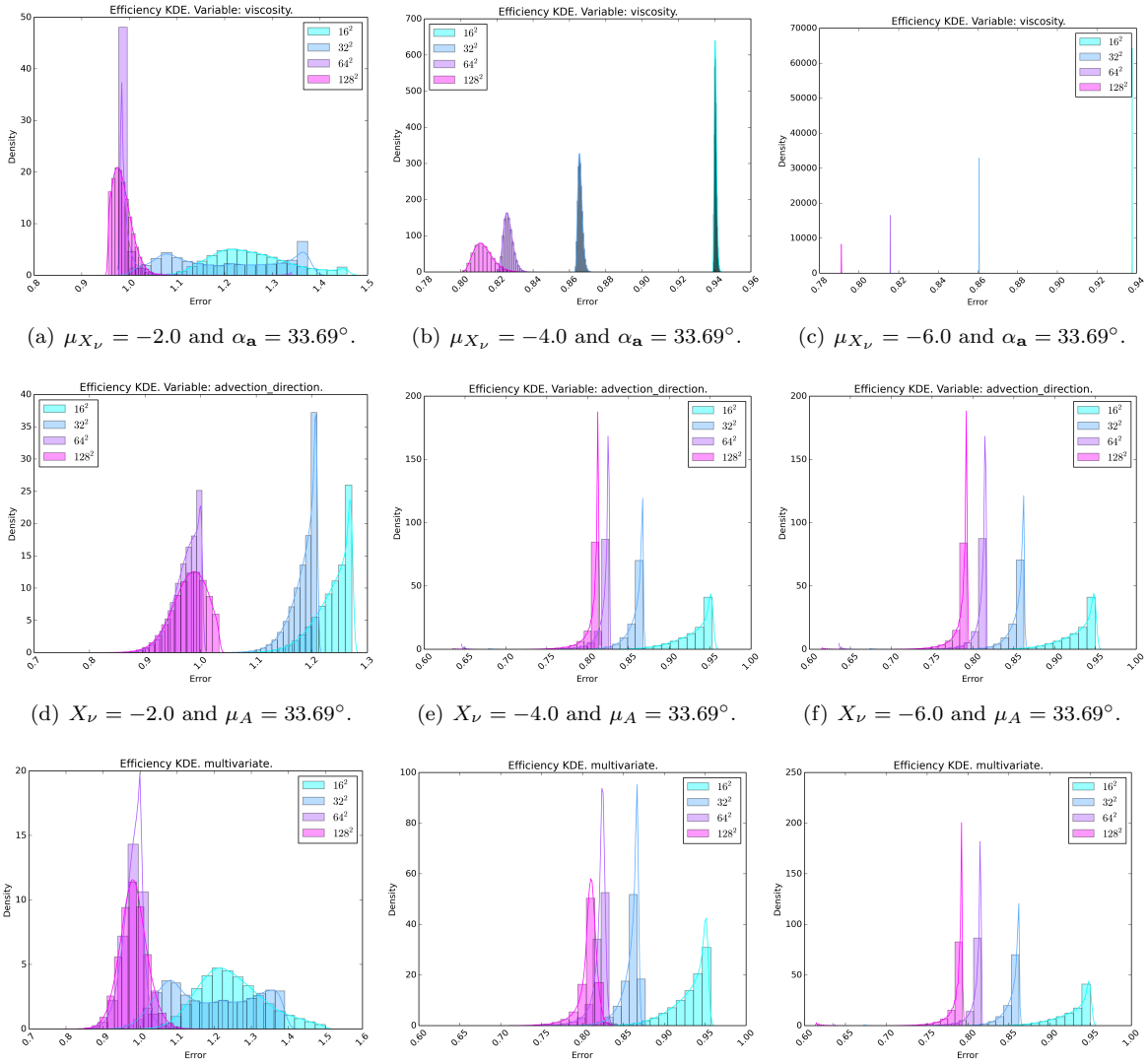

(a) $\mu_{X_\nu} = -2.0$ and $\alpha_{\mathbf{a}} = 33.69°$. (b) $\mu_{X_\nu} = -4.0$ and $\alpha_{\mathbf{a}} = 33.69°$. (c) $\mu_{X_\nu} = -6.0$ and $\alpha_{\mathbf{a}} = 33.69°$.

(d) $X_\nu = -2.0$ and $\mu_A = 33.69°$. (e) $X_\nu = -4.0$ and $\mu_A = 33.69°$. (f) $X_\nu = -6.0$ and $\mu_A = 33.69°$.

(g) $\mu_{X_\nu} = -2.0$ and $\mu_A = 33.69°$. (h) $\mu_{X_\nu} = -4.0$ and $\mu_A = 33.69°$. (i) $\mu_{X_\nu} = -6.0$ and $\mu_A = 33.69°$.

Figure 19: *Problem A*. Histogram and KDE for different mesh sizes with random viscosity (top row), random advection direction (middle row), and random viscosity and advection direction (bottom row).

these two viscosity values, the distribution of $\mathcal{I}_{\text{eff}}$ seems to converge towards the one obtained with 128^2 elements as the mesh is refined, with values concentrated near 0.80. For the case in which the viscosity is set to $\nu = 1.0e-2$ (left panel), the realizations of the efficiency index present higher amplitudes and variability.

When the stochastic viscosity and stochastic advection direction are both involved (bottom row), the results obtained for $\mu_{X_\nu} = -4.0$ (left panel) and $\mu_{X_\nu} = -6.0$ (right panel) are similar to those obtained with a deterministic viscosity (case (C2)), regardless of the mesh density. For $\mu_{X_\nu} = -2.0$ (left panel), the probability density functions of $\mathcal{I}_{\text{eff}}$ differ from those estimated with the univariate configurations (C1) and (C2). As expected from a physical viewpoint, these results suggest that for the manufactured polynomial solution (problem A), analyzing the viscous dominated regime necessitates that both the viscosity and the advection direction are made random, while the convection dominated case can be addressed by randomizing the advection direction only.

Similar conclusions can be drawn for the manufactured analytical solution with a boundary layer (problem B), for which results are shown in Figure 20. The results with a viscosity value of $\nu = 1.0e-6$

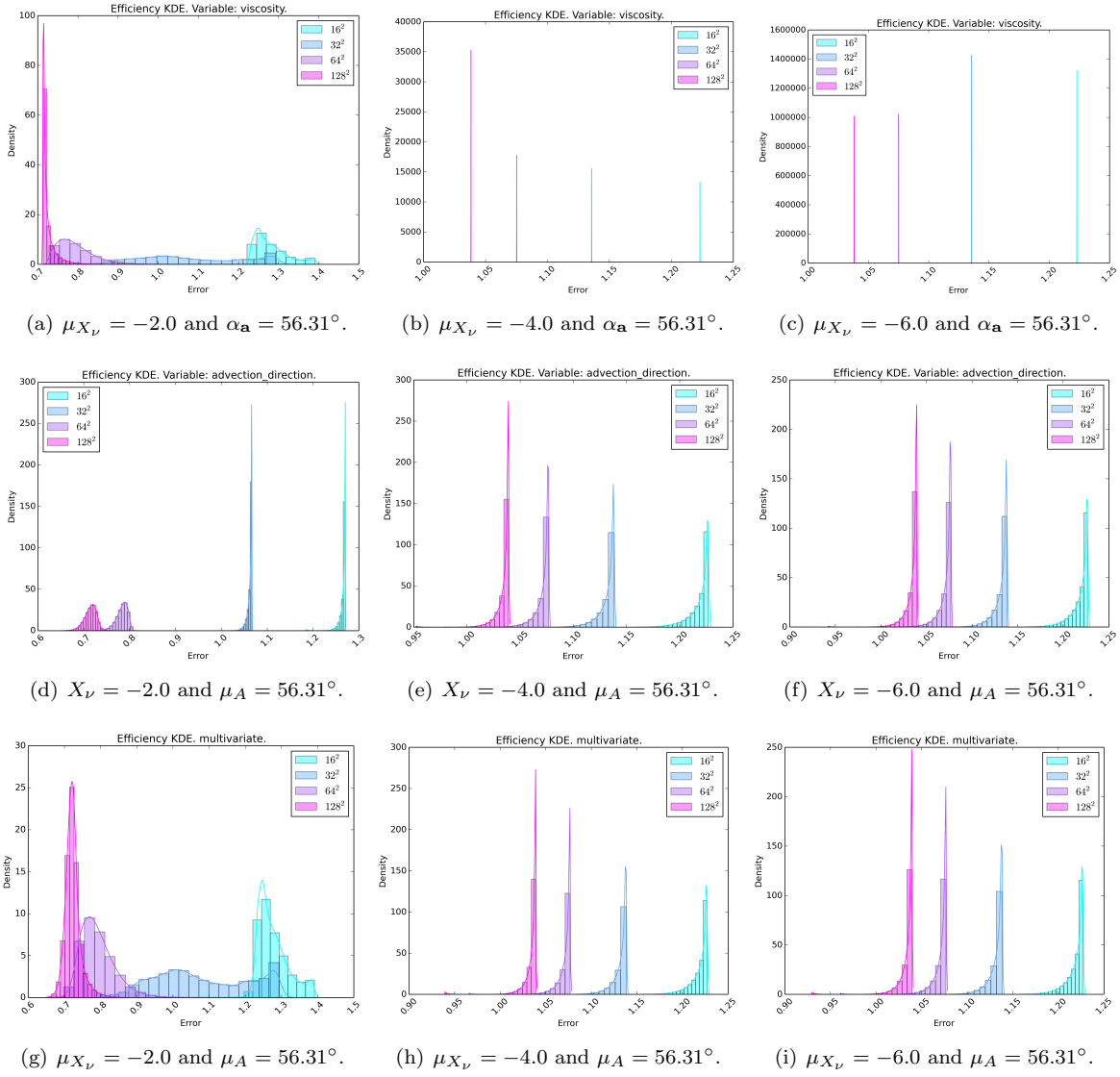

(a) $\mu_{X_\nu} = -2.0$ and $\alpha_{\mathbf{a}} = 56.31°$. (b) $\mu_{X_\nu} = -4.0$ and $\alpha_{\mathbf{a}} = 56.31°$. (c) $\mu_{X_\nu} = -6.0$ and $\alpha_{\mathbf{a}} = 56.31°$.

(d) $X_\nu = -2.0$ and $\mu_A = 56.31°$. (e) $X_\nu = -4.0$ and $\mu_A = 56.31°$. (f) $X_\nu = -6.0$ and $\mu_A = 56.31°$.

(g) $\mu_{X_\nu} = -2.0$ and $\mu_A = 56.31°$. (h) $\mu_{X_\nu} = -4.0$ and $\mu_A = 56.31°$. (i) $\mu_{X_\nu} = -6.0$ and $\mu_A = 56.31°$.

Figure 20: *Problem B.* Histogram and KDE for different mesh sizes with random viscosity (top row), random advection direction (middle row) and random viscosity and advection direction (bottom row).

(right panel) and $\nu = 1.0e-4$ (middle panel) are even closer than for the previous problem. Here, we also see that for the viscous dominated case (left panel), we have different efficiency distributions for the three cases considered (C1, C2 and C3). However, for the convection dominated cases (middle and right panels), the efficiency index is almost constant when the advection direction is deterministic (case (C1)) fixed, while cases (C2) and (C3) give same results.

Finally, in Figure 21, we depict the efficiency distributions for the circular inner layer test (problem C). For this problem, in the viscous dominated regime, the error estimator efficiency goes to zero as we refine the mesh, see Figure 6(b). This behavior is also observed in Figure 21, where for viscosity values of $\nu = 1.0e-2$ (left panel) we see that the distributions tend to a deterministic value close to zero as the mesh is refined. For the case of $\nu = 1.0e-4$ (middle panel), the efficiency values also decay, but at a

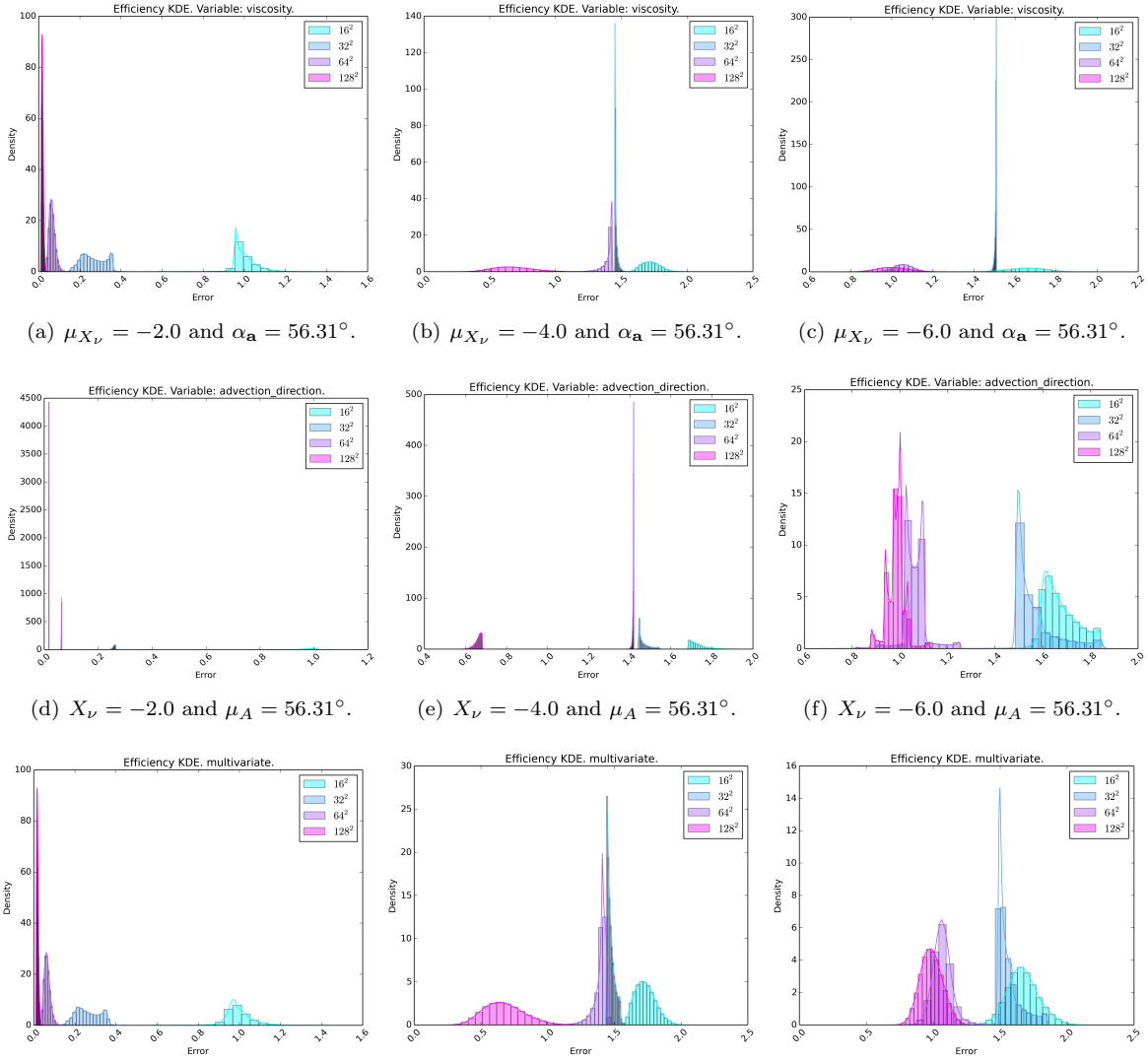

(a) $\mu_{X_\nu} = -2.0$ and $\alpha_{\mathbf{a}} = 56.31°$. (b) $\mu_{X_\nu} = -4.0$ and $\alpha_{\mathbf{a}} = 56.31°$. (c) $\mu_{X_\nu} = -6.0$ and $\alpha_{\mathbf{a}} = 56.31°$.

(d) $X_\nu = -2.0$ and $\mu_A = 56.31°$. (e) $X_\nu = -4.0$ and $\mu_A = 56.31°$. (f) $X_\nu = -6.0$ and $\mu_A = 56.31°$.

(g) $\mu_{X_\nu} = -2.0$ and $\mu_A = 56.31°$. (h) $\mu_{X_\nu} = -4.0$ and $\mu_A = 56.31°$. (i) $\mu_{X_\nu} = -6.0$ and $\mu_A = 56.31°$.

Figure 21: *Problem C.* Histogram and KDE for different mesh sizes with random viscosity (top row), random advection direction (middle row) and random viscosity and advection direction (bottom row).

lower rate. In that case, we observe that the variability of efficiency values for meshes with 32^2 and 64^2 elements is less important than the variability of meshes with 16^2 and 128^2 elements, for the three cases considered (C1, C2 and C3). Also note that for the middle panel, the distributions for meshes 64^2 and 128^2 elements are far apart, implying that in this regime the effect of the mesh size is important. This behavior is not observed for the case with $\nu = 1.0e-6$ (right panel), where the efficiency distributions for the two finest meshes are close. Here, also according to the results shown in Figure 6(d), the efficiency distributions tend to values close to 1.0.

6. Conclusions

We have defined a new *a posteriori* error estimator based on the VMS approach using orthogonal subscales for the CDR problem. The error estimator is defined in the L^r-norm and is constructed from

the L^∞-norm of the orthogonal projection of the residual and the inter-element fluxes.

The robustness of the proposed error estimator and an existing VMS error estimator have been extensively assessed for three different manufactured analytical solutions. We have analyzed the evolution of the efficiency index as the mesh is refined for viscous-dominated and convection-dominated regimes. Similar results are obtained for the proposed and existing error estimators, with values of efficiency index close to 1.0 for the proposed error estimator as we refine the mesh, especially for convection-dominated regimes.

A parametric study has been carried out for one of the benchmarks with respect to physical properties and mesh discretization. The result of this study was that the error estimator may be a non-smooth function of the varying parameters.

We have also evaluated the impact of system-parameter uncertainties on the proposed error estimator. In this regard, the convergence analysis of the uncertainty propagation method revealed that the non-smoothness of the error estimator response as a function of the input variables (viscosity or advection direction) significantly affects the convergence of the PCE. Further, we have compared the distributions of the exact and estimated error when uncertain viscosity and advection direction are considered. Finally, we have analyzed the efficiency index probability distributions obtained for the three benchmarks considered under different probabilistic settings.

Acknowledgements

Support for this research was provided by the Defense Advanced Research Projects Agency (DARPA) program on Enabling Quantification of Uncertainty in Physical Systems (EQUiPS) led by Dr. Fariba Fahroo, Program Manager. The authors would also like to thank Dr. Pietro Congedo at INRIA-Bordeaux/Sud-Ouest, Prof. Omar Knio at Duke University and Prof. Olivier Le Maître at LIMSI for valuable discussions and suggestions.

References

[1] I. Celik, M. Klein, M. Freitag, J. Janicka, Assessment measures for URANS/DES/LES: an overview with applications, Journal of Turbulence 7 (2006) N48.

[2] R. Ghanem, D. Higdon, H. Owhadi, Handbook of Uncertainty Quantification, Springer, 2017.

[3] P. J. Roache, Quantification of uncertainty in computational fluid dynamics, Annual Review of Fluid Mechanics 29 (1) (1997) 123–160.

[4] J. T. Oden, I. Babuška, F. Nobile, Y. Feng, R. Tempone, Theory and methodology for estimation and control of errors due to modeling, approximation, and uncertainty, Computer Methods in Applied Mechanics and Engineering 194 (2) (2005) 195–204.

[5] R. Rebba, S. Mahadevan, S. Huang, Validation and error estimation of computational models, Reliability Engineering & System Safety 91 (10) (2006) 1390–1397.

[6] C. Roy, Review of discretization error estimators in scientific computing, 48th AIAA Aerospace Sciences Meeting Including the New Horizons Forum and Aerospace Exposition.

[7] L. Eça, M. Hoekstra, A procedure for the estimation of the numerical uncertainty of CFD calculations based on grid refinement studies, Journal of Computational Physics 262 (2014) 104–130.

[8] I. Babuška, W. C. Rheinboldt, A-posteriori error estimates for the finite element method, International Journal for Numerical Methods in Engineering 12 (10) (1978) 1597–1615.

[9] M. Ainsworth, J. T. Oden, A Posteriori Error Estimation in Finite Element Analysis, John Wiley & Sons, 2011.

[10] R. Verfürth, R. V. Urth, A posteriori error estimates for nonlinear problems. finite element discretizations of parabolic equations, Mathematics of Computation 62.

[11] G. Hauke, M. H. Doweidar, M. Miana, The multiscale approach to error estimation and adaptivity, Computer Methods in Applied Mechanics and Engineering 195 (13) (2006) 1573–1593.

[12] T. J. R. Hughes, Multiscale phenomena: Green's functions, the Dirichlet-to-Neumann formulation, subgrid scale models, bubbles and the origins of stabilized methods, Computer Methods in Applied Mechanics and Engineering 127 (1) (1995) 387–401.

[13] G. Hauke, D. Fuster, M. H. Doweidar, Variational multiscale a-posteriori error estimation for multi-dimensional transport problems, Computer Methods in Applied Mechanics and Engineering 197 (33) (2008) 2701–2718.

[14] G. Hauke, D. Fuster, F. Lizarraga, Variational multiscale a posteriori error estimation for systems: The Euler and Navier-Stokes equations, Computer Methods in Applied Mechanics and Engineering 283 (2015) 1493–1524.

[15] D. Irisarri, G. Hauke, A posteriori pointwise error computation for 2-D transport equations based on the variational multiscale method, Computer Methods in Applied Mechanics and Engineering 311 (2016) 648–670.

[16] O. Colomés, G. Scovazzi, I. Sraj, O. Knio, O. L. Matre, A finite volume error estimator inspired by the variational multiscale approach, 2018 AIAA Non-Deterministic Approaches Conference.

[17] R. Codina, Stabilization of incompressibility and convection through orthogonal sub-scales in finite element methods, Computer Methods in Applied Mechanics and Engineering 190 (13) (2000) 1579–1599.

[18] J. Baiges, R. Codina, Variational multiscale error estimators for solid mechanics adaptive simulations: An orthogonal subgrid scale approach, Computer Methods in Applied Mechanics and Engineering 325 (2017) 37–55.

[19] R. Codina, On stabilized finite element methods for linear systems of convection-diffusion-reaction equations, Computer Methods in Applied Mechanics and Engineering 188 (1) (2000) 61–82.

[20] L. P. Franca, F. Valentin, On an improved unusual stabilized finite element method for the advective-reactive-diffusive equation, Computer Methods in Applied Mechanics and Engineering 190 (13) (2000) 1785–1800.

[21] G. Hauke, A simple subgrid scale stabilized method for the advection-diffusion-reaction equation, Computer Methods in Applied Mechanics and Engineering 191 (27) (2002) 2925–2947.

[22] O. Colomés, S. Badia, R. Codina, J. Principe, Assessment of variational multiscale models for the large eddy simulation of turbulent incompressible flows, Computer Methods in Applied Mechanics and Engineering 285 (2015) 32–63.

[23] B. N. Granzow, M. S. Shephard, A. A. Oberai, Output-based error estimation and mesh adaptation for variational multiscale methods, Computer Methods in Applied Mechanics and Engineering 322 (2017) 441–459.

[24] T. J. R. Hughes, G. R. Feijóo, L. Mazzei, J.-B. Quincy, The variational multiscale methoda paradigm for computational mechanics, Computer Methods in Applied Mechanics and Engineering 166 (1) (1998) 3–24.

[25] G. Hauke, M. H. Doweidar, M. Miana, Proper intrinsic scales for a-posteriori multiscale error estimation, Computer Methods in Applied Mechanics and Engineering 195 (33) (2006) 3983–4001.

[26] G. Sangalli, Robust a-posteriori estimator for advection-diffusion-reaction problems, Mathematics of Computation 77 (261) (2008) 41–70.

[27] T. Hughes, G. Sangalli, Variational multiscale analysis: the finescale Greens function, projection, optimization, localization, and stabilized methods, SIAM Journal on Numerical Analysis 45 (2) (2007) 539–557.

[28] S. Badia, A. F. Martn, J. Principe, FEMPAR: An object-oriented parallel finite element framework, Archives of Computational Methods in Engineering (2017) 1–77.

[29] V. John, A numerical study of a posteriori error estimators for convection-diffusion equations, Computer Methods in Applied Mechanics and Engineering 190 (5) (2000) 757–781.

[30] S. B. Pope, Turbulent Flows, Cambridge University Press, 2000.

[31] E. Jaynes, Information theory and statistical mechanics i, Physical Review 106 (4) (1957) 620–630.

[32] E. Jaynes, Information theory and statistical mechanics ii, Physical Review 108 (2) (1957) 171–190.

[33] C. E. Shannon, A mathematical theory of communication., Bell System Technical Journal 27 (1948) 379–423/623–659.

[34] N. Wiener, The homogeneous chaos, American Journal of Mathematics 60 (4) (1938) 897–936.

[35] R. H. Cameron, W. T. Martin, The orthogonal development of non-linear functionals in series of fourier-hermite functionals, Annals of Mathematics 48 (2) (1947) 385–392.

[36] D. Xiu, G. Karniadakis, The Wiener–Askey polynomial chaos for stochastic differential equations, SIAM Journal on Scientific Computing 24 (2) (2002) 619–644.

[37] O. Le Maître, O. M. Knio, H. N. Najm, R. G. Ghanem, Uncertainty propagation using wienerhaar expansions, Journal of Computational Physics 197 (1) (2004) 28–57.

[38] O. Le Maître, O. M. Knio, Spectral Methods for Uncertainty Quantification: With Applications to Computational Fluid Dynamics, Springer Science & Business Media, 2010.

[39] M. Arnst, R. Ghanem, E. Phipps, J. Red-Horse, Reduced chaos expansions with random coefficientsin reduced-dimensional stochastic modeling of coupled problems, International Journal for Numerical Methods in Engineering 97 (5) (2014) 352–376.

[40] P. Constantine, M. S. Eldred, E. T. Phipps, Sparse pseudospectral approximation method, Computer Methods in Applied Mechanics and Engineering 229–232 (2012) 1–12.

[41] B. Adams, L. Bauman, W. Bohnhoff, K. Dalbey, M. Ebeida, J. Eddy, M. Eldred, P. Hough, K. Hu, J. Jakeman, J. Stephens, L. Swiler, D. Vigil, T. Wildey, Dakota, a multilevel parallel Object-Oriented framework for design optimization, parameter estimation, uncertainty quantification, and sensitivity analysis: Version 6.0 users manual (2014).

[42] H. N. Najm, Uncertainty quantification and polynomial chaos techniques in computational fluid dynamics, Annual Review of Fluid Mechanics 41 (1) (2009) 35–52.

[43] R. Codina, Analysis of a stabilized finite element approximation of the oseen equations using orthogonal subscales, Applied Numerical Mathematics 58 (3) (2008) 264–283.

Appendix A. Definition of the orthogonal projection

The selection of the space for the approximation of the subscales determines the projection $\mathcal{P}$ appearing in the right-hand side of (14). The first option, which has been denoted as *standard VMS* in this work, is to take the subscales in the space of the residuals, that is,

$$\mathcal{P} := \mathcal{I}. \tag{A.1}$$

This option was already considered in [24] and named Algebraic Subgrid Scale (ASGS) in [17].

Another possibility introduced in [17] is to consider the space of the subscales orthogonal to the FE space. The main motivation of the method is that a stability estimate for the projection onto the FE space of the convective term can already be obtained in the standard Galerkin method and therefore the only "missing" part is the orthogonal one. The Orthogonal Subscales (OSS) method is then characterized by the following projection definition:

$$\mathcal{P} := \Pi_h^{\perp} = \mathcal{I} - \Pi_h, \tag{A.2}$$

where Π_h is the L^2-projection onto the FE, $\mathcal{V}_h$, space given by

$$(\Pi_h(w), v_h) = (w, v_h) \quad \forall v_h \in \mathcal{V}_h. \tag{A.3}$$

With this choice, the orthogonality between the space of subscales and the FE space is only guaranteed when the stabilization parameters are constant. Otherwise, when this condition is not satisfied, the method is still optimally convergent, but the orthogonality property is lost. In order to enforce orthogonal subscales, a slight modification of the projection Π_h is needed. That is the use of a weighted projection, Π_τ.

Note that we project onto the space $\mathcal{V}_h$, but we could also compute the projection onto $\mathcal{V}_{0,h}$. However, according to [43], this last option could lead to spurious numerical boundary layers.

Given any scalar $w \in \mathcal{V}$, the weighted projection Π_τ is defined by

$$(\tau\Pi_\tau(w), v_h) = (\tau w, v_h) \quad \forall v_h \in \mathcal{V}_h. \tag{A.4}$$

Using the weighted projection (A.4), the approximation equivalent to (14) would read

$$u' \approx \tau\Pi_\tau^{\perp}(f - \mathcal{L}u_h) = \tau\left(f - \mathcal{L}u_h - \xi_h\right), \tag{A.5}$$

where $\xi_h := \Pi_\tau\left(f - \mathcal{L}u_h\right)$ is the projection of the residual $(f - \mathcal{L}u_h)$ into the finite element space $\mathcal{V}_h$. With these definitions, the discrete problem (16) can be reformulated as: find $[u_h, \xi_h] \in \mathcal{V}_{0,h} \times \mathcal{V}_h$ such that

$$a(u_h, v_h) + \sum_{K\in\mathcal{T}_h} \left(\tau\left(f - \mathcal{L}u_h - \xi_h\right), \mathcal{L}^* v_h\right)_K = (f, v_h) + (v_h, h)_{\Gamma_h} \qquad \forall v_h \in \mathcal{V}_{0,h}, \tag{A.6a}$$

$$(\tau\xi_h, w_h) = (\tau(f - \mathcal{L}u_h), w_h) \qquad \forall w_h \in \mathcal{V}_h. \tag{A.6b}$$

Appendix B. Error estimators computation algorithm

The error estimators used in this work, η_K^{OSS} and η_K^{VMS}, are given by equations (32) and (33), respectively. Since they are explicit *a posteriori* error estimators, its computation can be easily done once the numerical solution of the problem, u_h, is obtained, following the steps described in Algorithm 1.

Algorithm 1 VMS error estimator computation

Solve the CDR problem (16) using (17) for the OSS method, or (14), with $\mathcal{P} \equiv \mathcal{I}$ for the VMS method
Result: u_h (and $\Pi_h(\mathcal{L}u_h - f)$ for the OSS method)
for $K \in \mathcal{T}_h$ **do**
    Evaluate $\|f - \mathcal{L}u_h\|_{L^\infty(K)}$ (or $\|f - \mathcal{L}u_h - \Pi_h(f - \mathcal{L}u_h)\|_{L^\infty(K)}$ for OSS)
    Evaluate $\|[\![\mathcal{B}u_h]\!]\|_{L^\infty(K)}$
    Evaluate meas(K)
    Evaluate meas(∂K)
    Evaluate $\tau_{L^2}^K := \min\left(\frac{h_{flow}}{\sqrt{3}|\mathbf{a}|}, \frac{h^2}{24.24\nu}, \frac{1}{|s|}\right)$
    Compute η_K^{OSS} or η_K^{VMS}, using (32) or (33), respectively
    Add contribution to η
end for
Resutl: Global error estimator η